Metamorphic evolution of the western Gawler Craton

Thesis submitted in accordance with the requirements of the University of Adelaide for an Honours Degree in Geology/Geophysics

Philippe Dupavillon

November 2015

THE UNIVERSITY of ADELAIDE

TITLE: METAMORPHIC EVOLUTION OF THE WESTERN GAWLER CRATON
RUNNING TITLE: METAMORPHISM OF THE WESTERN GAWLER CRATON

ABSTRACT

The tectonothermal evolution of the western Gawler Craton, including the Fowler Domain, during Proterozoic Australia is currently poorly understood. *In-situ* U-Pb ages obtained in this study from the Fowler Domian yielded ages of metamorphism at c. 1732–1701 Ma attributed to the Kimban Orogeny, and at c. 1599 Ma attributed to Kararan/Hiltiba events. Quantitative phase equilibria modelling, i.e. pressure-temperature pseudosections, provide the first modern metamorphic constraints on pressure–temperature conditions for two areas within the Fowler Domain and are ~2.6–7.4 kbar and 550– 700°C for the Barton Block, and 8.2–8.7 kbar and 450– 475°C for the Nundroo Block which equate to apparent thermal gradients of approximately ~116–135°C /kbar and ~50–60 °C/kbar respectively. These thermal gradients occur within the hotter part of the 'high *T*/*P* or Barrovian' (Barton Block) and 'colder than normal' (or eclogite–high-pressure granulite, Nundroo Block) subdivisions of *P*–*T* space. This is suggestive of extension in the Barton Block and later convergence in the Nundroo Block. Kimban-aged tectonism in other parts of the Gawler Craton records thermal gradients ranging between ~150–133 °C/kbar. These differences in thermal gradients are appreciably, and in some cases different from previous studies on the Fowler Domain. The Curnamona Province (north-north eastern South Australian Craton) possesses sedimentation and thermal gradients consistent with divergence within this time period. This has prompted many scientific debates surrounding tectonic regime of the Proterozoic time line, which are yet to include any metamorphic quantitative pressure-temperature considerations. Apparent thermal gradients presented in this study are consistent with both divergence within the Kimban Orogenisis time line 1730–1690 Ma, and convergence within Kararn-/Hiltiba time line 1600–1550Ma. These processes are interpreted to record Tasmanide type tectonic regimes.

KEYWORDS

U–Pb geochronology, P–T pseudosection, geothermal gradients, Proterozoic Australia, Tectonics

TABLE OF CONTENTS

LIST OF FIGURES

LIST OF TABLES

1. INTRODUCTION

Much effort has been devoted to proposing tectonic models for the growth, evolution and assembly of the Proterozoic parts of Australia (Myers *et al.*, 1996; Giles *et al.*, 2004; Giles *et al.*, 2006; Wade *et al.*, 2006; Payne *et al.*, 2009; Kirkland *et al.*, 2011; Smithies *et al.*, 2011; Pisarevsky *et al.*, 2014). Critical inputs for such models of fundamental data, such as the metamorphic age and metamorphic character of different crustal domains, are lacking. The Gawler Craton in South Australia has preserved margins in the east, north and west (the south faces the Southern Ocean), and thus these areas comprise critical regions for continent and supercontinent assembly models. However, efforts to extract fundamental data from these regions in order to test and refine large-scale tectonic models are hampered by the obscuring presence of much younger sedimentary cover. In such regions data can typically be collected from sparsely distributed drill holes that intersect crystalline basement (Teasdale, 1997). The Fowler Domain in the western Gawler Craton, Figures 1 and 2, is the focus of study for this project. To date, modern metamorphic pressure–temperature data does not exist for the Fowler Domain, however metamorphic age has been constrained in Howard *et al.* (2011a). Based on data collected in this study, the age of metamorphism in the Fowler Domain further constrains an event that is widely known as a period of major tectonism in the Gawler Craton and elsewhere in Proterozoic Australia. Constraints from data collected in this study, in combination with existing data from other parts of the Gawler Craton and Proterozoic Australia, allow for an appraisal of the tectono-metamorphic regime at that time, with implications for models of the assembly of Proterozoic Australia.

In this study, samples from diamond drill hole core are used to obtain Laser Ablation Inductively Coupled Plasma Mass Spectrometry (LA–ICP–MS) monazite U–Pb geochronological data as well as metamorphic pressure–temperature (P–T) data using the modern approach of calculated phase equilibria forward models (i.e. pseudosections), with the primary aim of constraining the age and

thermal regime (as apparent thermal gradient) of metamorphism in the Fowler Domain, for the purpose of placing possible constraints on the tectonic setting at the time of metamorphism. Additionally this work will be discussed in the context of existing data and models for the tectonic setting of the Gawler Craton and other parts of Proterozoic Australia.

2. GEOLOGICAL BACKGROUND

2.1 Regional geology

The crystalline basement of much of South Australia is known as the Gawler Craton and is comprised of late Archean to early Mesoproterozoic rocks. The craton records a complex tectonic history involving numerous major events spanning the period c. 2450 Ma to c. 1450 Ma (Fanning *et al.*, 1988; Teasdale, 1997; Thomas *et al.*, 2008; Boger, 2011; Payne *et al.*, 2009; Fraser and Lyons, 2006), including at least four major tectono-metamorphic and/or magmatic events (Dutch *et al.*, 2010; Hand *et al.*, 2007) and is summarised in Table 1.

The Gawler Craton's geology is difficult to study due to its remoteness, inaccessible Native Title Claims, and regionally extensive (10s–100s m) thick regolith cover. The southern margin of the Gawler Craton is considered to be the continental shelf beneath the Southern Ocean, and was once contiguous with Antarctica's East Antarctica shield prior to Gondwana supercontinent break up in the Cretaceous (Peucat *et al.*, 1999; Sayers *et al.*, 2001; Fraser, 2010; Payne *et al.*, 2009; Boger, 2011). Due to significant sedimentation in the Neoproterozoic to Phanerozoic Officer Basin, the nature of the west, northwest, and northeast boundaries of the Gawler Craton are not clearly understood (Teasdale, 1997).

Table 1. Summary of events within the Gawler Craton during time interval c. 2500–1450 Ma, adapted after Reid *et al.* (2008). References for each time line (a-e) are numbered 1.–20. as follows: 1.= (Reid *et al.*, 2014b), 2.= (Daly and Fanning, 1993), 3.= (Reid *et al.*, 2014a), 4.= (Fanning *et al.*, 1981), 5.= (Fanning *et al.*, 1988), 6.= (Duclaux *et al.*, 2007), 7.=(Fanning *et al.*, 2007), 8.= (Howard *et al.*, 2009), 9.= (Reid *et al.*, 2008), 10.= (Mortimer *et al.*, 1988), 11.= (Szpunar *et al.*, 2011), 12.= (Howard *et al.*, 2011a), 13.= (Hand *et al.*, 2007), 14.= (Barovich and Hand, 2008), 15.= (Flint *et al.*, 1993), 16.= (Allen *et al.*, 2008), 17.= (Conor, 1995), 18.= (Cutts *et al.*, 2011), 19.= (Forbes *et al.*, 2011), 20.= (Fraser and Lyons, 2006).

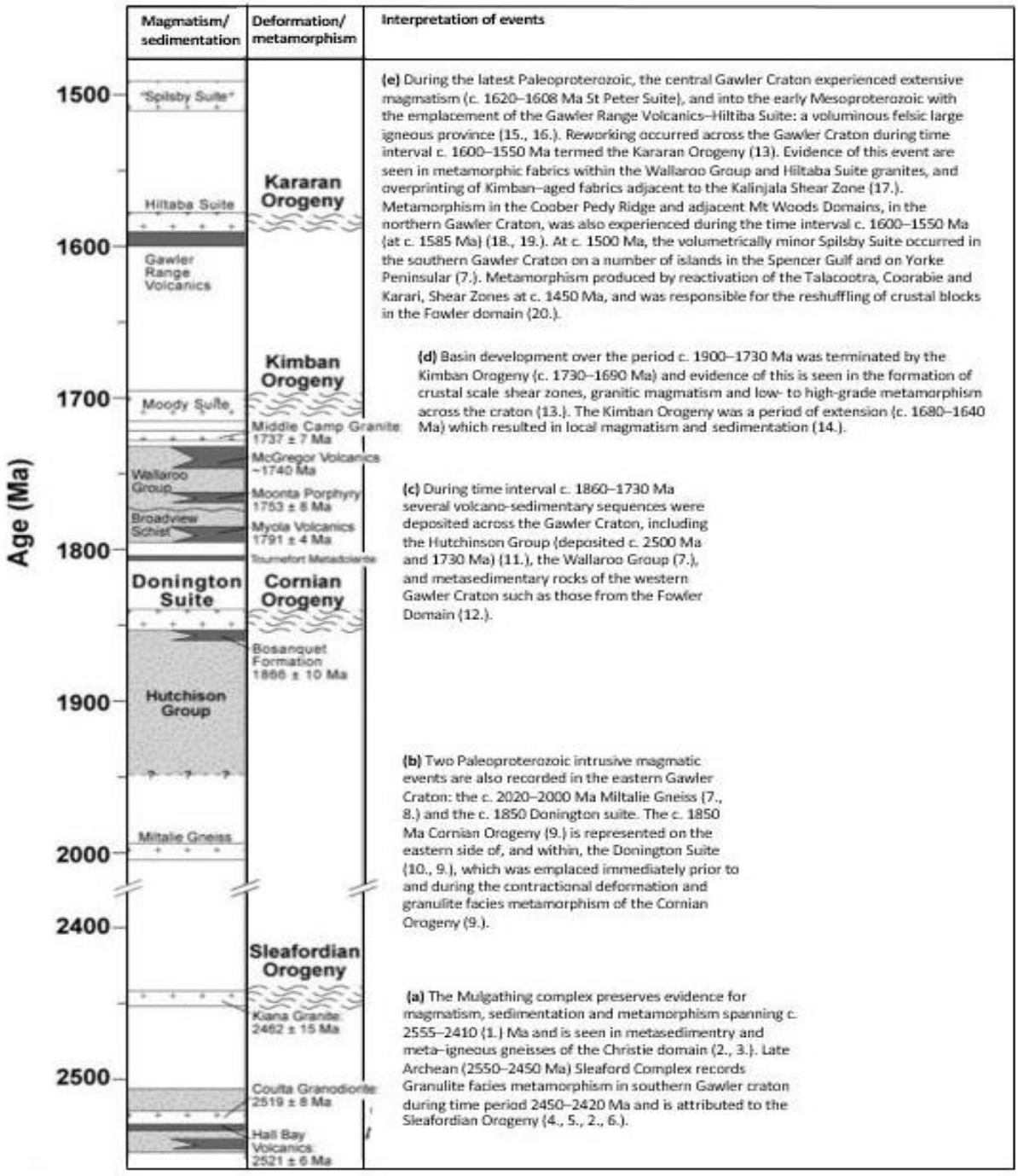

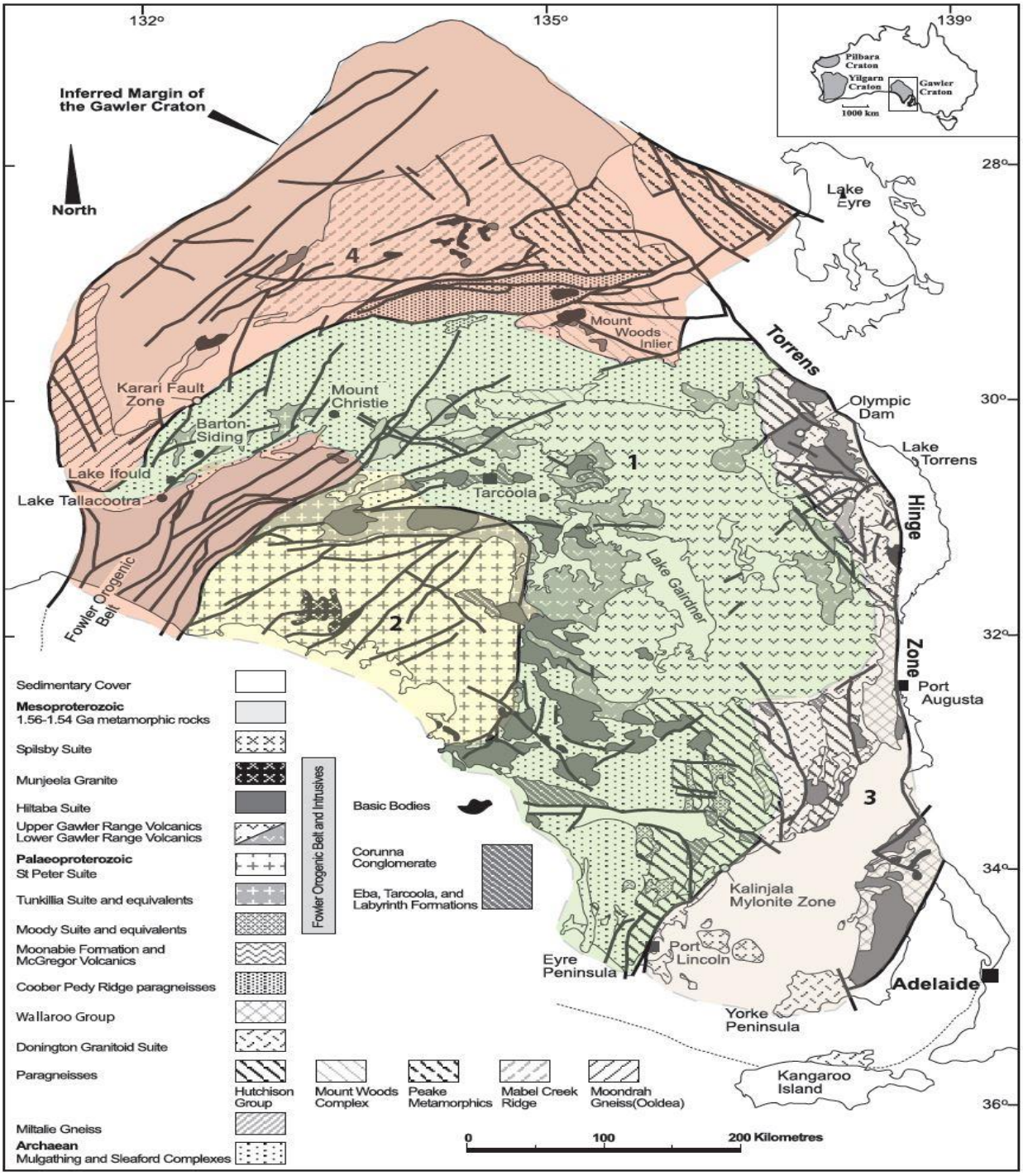

Figure 1. Simplified interpreted subsurface geology of the Gawler Craton, South Australia, with simplified domains based on geological associations. 1 (green) Central Domain, 2 (yellow) South-west domain, 3 (light pink) Olympic Domain, 4 (dark pink) North-west Domain (adapted after: Daly *et al.*, 1998b; Swain *et al.*, 2005; Dutch, 2009).

2.2 Fowler Domain

The Fowler Domain in the western Gawler Craton (Figures 1,2) forms a geophysically distinctive, NNE to NE trending belt of magnetic metamorphic and igneous rocks, dissected by a number of anastomosing shear zones (Teasdale, 1997; Daly *et al.*, 1998b). These Paleoproterozoic rocks have undergone poly-metamorphism through late Paleoproterozoic and Mesoproterozoic deformation events (Teasdale, 1997; Hand *et al.*, 2007; Howard *et al.*, 2011a). The Fowler Domain is bounded by the Christie Domain to the north and west, and by the Palaeo–Mesoproterozoic Wilgena and Nuyts Domains to the east. The area is bordered to the west and north, by the Karari Shear Zone and a branch of the Tallacootra Shear Zone which defines a boundary between late Archean to earliest Paleoproterozoic rocks (Fraser *et al.*, 2012), and to the east by the Coorabie Shear Zone (Figure 2; Teasdale, 1997).

The intense magnetic signature of the Fowler Domain can be attributed to a variety of rocks with high magnetic susceptibilities obtained from and attributed to mafic and ultramafic intrusives (Daly *et al.*, 1994; Morris *et al.*, 1994; Teasdale, 1997), as well as intermediate–felsic igneous and metasedimentary rocks (Teasdale, 1997; Howard *et al.*, 2011a). The known geology of the Fowler Domain is based on very limited coastal out crop (Teasdale, 1997) and sparsely distributed diamond drill core. However, geophysical work, based on magnetics and gravity signatures, divided the Fowler Domain into four blocks that from east to west are the Nundroo, Central, Barton and Colona Blocks (Figure 2; Teasdale, 1997). Although these blocks have approximately similar magnetic and gravity signatures, their known geological characteristics, in particular metamorphic grade, differ significantly (Teasdale, 1997). Previous research has produced important data (Table 2) from samples within the Fowler Domain, such as maximum depositional ages of sedimentation, age of metamorphism and conventional thermobarometric estimates of *P–T* conditions (expressed as apparent thermal gradient data in Table 2). As shown in Table 2, the age of metamorphism, as

determined using monazite and/or zircon geochronology (Teasdale, 1997; Thomas *et al.*, 2008; Howard *et al.*, 2011a) is mostly that of the Kimban Event (c. 1730–1690 Ma), with lesser documentation of the Kararan (c. 1600–1550 Ma) and other unknown timelines (e.g. 1635 ± 9 Ma, 1664 ± 7 Ma, 1505 ± 14 Ma; Thomas *et al.*, 2008; Howard *et al.*, 2011a). Tectonic regime in the region during the Kimban Orogen (1730–1690 Ma) remains unclear (Fraser *et al.*, 2012). The following is a summary of the known information about the blocks within the Fowler Domain which has been collected and presented in this study.

2.2.1 Nundroo Block

The Nundroo Block (Figure 2) comprises intermediate to mafic gneisses interlayered with metapelitic gneiss, both of which are overprinted by mylonite and ultramylonite zones (Teasdale, 1997). The mafic lilthologies are intrusive within the metasedimentry rocks, and these range from weakly deformed, coarse-grained diorites and gabbros, through to high-metamorphic-grade mafic granulites, and well-foliated hornblende and/ or biotite-rich amphibolites (Teasdale, 1997). The high-grade lithologies are intruded by very coarse-grained pegmatites. Existing metamorphic age data from metapelitic gneiss used the chemical (not isotopic) electron probe micro analysis (EPMA) method to produce a weighted mean U–Th–Pb monazite age of 1471 ± 14 Ma (Thomas *et al.*, 2008), later recalculated by Dutch *et al.* (2010) to give 1505 ± 14 Ma. The thermal gradient of metamorphism is constrained at ~55–87.5 °C/kbar on the basis of *P–T* results from conventional thermobarometry (Teasdale, 1997). There are no constraints on the maximum deposition age of sediments in this Block.

2.2.2 Central Block

This Block is approximately 10–20 km wide and more than 200 km long (Figure 2). The lithologies here are lower in magnetic intensity than the other blocks in the Fowler Domain, and this has been attributed to its felsic intrusive rocks with only minor mafic influence (Teasdale, 1997). Two suites of different interpreted age of variably deformed granitoids have been identified. The older suite has a magmatic zircon SHRIMP U–Pb age of 1672 ± 12 Ma (Teasdale, 1997).

2.2.4 Colona Block

The Colona Block is approximately 30 km wide and narrows to the northeast (Figure 2). This block comprises a series of variably metamorphosed and deformed, strongly magnetised, layered, intermediate to mafic intrusive igneous rocks (Teasdale, 1997). These rocks show compositional range from biotite-rich tonalities and granodiorites through to hornblende-bearing gabbros and metasediments. Earlier coarse-grained assemblages and fabrics have been transposed to form new, finer-grained retrograde fabrics (Teasdale, 1997). Fine– to medium–grained, un-deformed granite crosscuts the deformed intrusives. Pegmatites and small scale (1 cm to 1 m wide) cataclastic shear zones crosscut all lithologies and are associated with chlorite–sericite alteration. Metamorphic age constraints from metasediments using LA–ICP–MS monazite U–Pb geochronology are 1695 ± 18 Ma and 1690 ± 9 Ma (Table 2; Howard *et al.*, 2011a) and using EPMA are more variable, 1688 ± 13 Ma, 1683 ± 12 Ma and 1649 ± 12 Ma (Table 2; Thomas *et al.*, 2008). Metamorphic zircon ages (U–Pb SHRIMP) from mildly deformed, coarse grained, and layered hornblende gabbro are 1730 ± 10 Ma (Teasdale, 1997). These data clearly indicate the Colona Block to record Kimban-aged metamorphism. The maximum age of sedimentation was constrained by U–Pb dating of detrital zircon in one metasediment to be 1760 ± 14 Ma (Howard *et al.*, 2011a).

2.2.3 Barton Block

This block is sigmoidal in shape, is up to 30 km wide and more than 200 km long (Figure 2). The main lithologies characterising the drill core of this Block are: mafic gneisses, metasedimentry schists and gneisses, and granitoids. Mylonitic textures occur in the main lithologies. A single metamorphic monazite U–Th–Pb age from metapelitic gneiss this block gave 1712 ± 9.5Ma (i.e. Kimban age) by the chemical EMPA method (Teasdale, 1997). The thermal gradient of metamorphism is constrained at ~83–130 °C/kbar on the basis of *P–T* results from conventional thermobarometry (Teasdale, 1997). The maximum age of sedimentation was constrained by U–Pb dating of detrital zircon in two samples to be 1738 ± 15 Ma and 1717 ± 11 Ma (Howard *et al.*, 2011a).

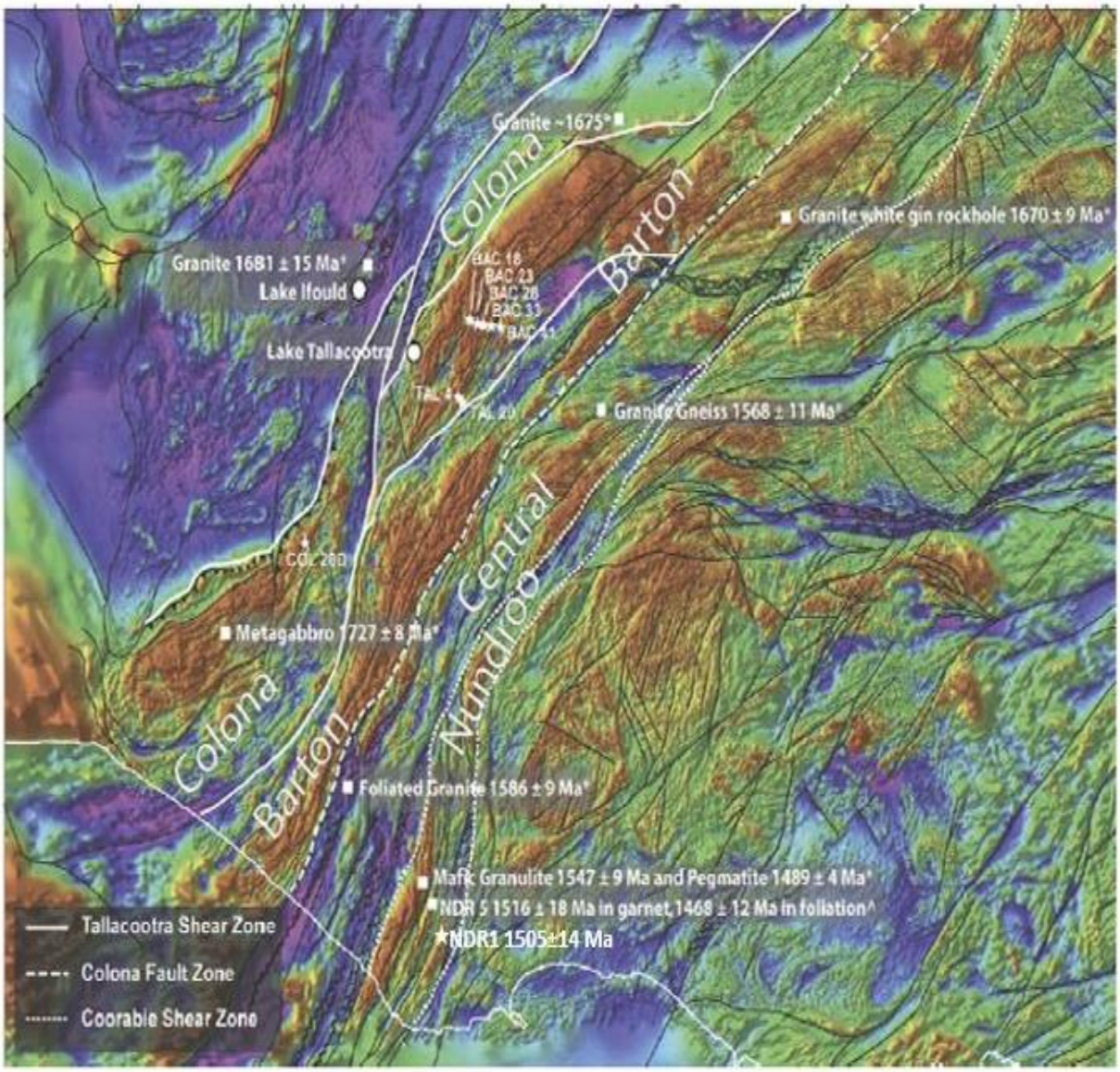

Figure 2. Total magnetic intensity image of the western Gawler Craton including the Fowler Domain and interpreted major shear zones bounding its four blocks (Nundroo, Central, Barton and Colona). The Fowler Domain lies between the Tallacootra (in NW) and Coorabie (in SE) Shear Zones. Drill hole samples used in this study (BAC23, BAC28, NDR1) are displayed and labelled. Previously collected age data and drill holes are displayed, by Swain *et al.* (2005), Boger (2011).

Table 2. Summary of previous and current data from the Fowler Domain. COL= Colona Block, TAL= Talacootra shear zone, BAC= Barton Block, NDR= Nudroo Block, a=Howard *et al.* (2011a), b= Teasdale (1997), c= Thomas *et al.* (2008) in Howard *et al.* (2011a) and d= this study.

Drill hole and Sample number	Whole rock geochemistry	*P–T* pseudosection	Constraints on maximum depositional age (U–Pb zircon)	Metamorphic age, monazite (mnz) or zircon (z), using EMPA (recalculated by Dutch *et al.* (2010) in (a) and LA–ICP–MS U–Pb methods	EPMA Garnet compositional traverses	Thermal gradient calculations °C/kbar	Petrographic description	Total radiogenic heat production calculations (μW m^{-3})
COL20D 46.6-47.5m	(a)		(a) 1760±14Ma (2σ, n=13, z)	(a) 1695±18Ma(2σ, n=5,z), 1690±9Ma (LA-ICP-MS, 2σ, n=20mnz)			(d) gt-bi-mu-q-pl-ilm-sill	(d) 2.88
COL20D 44m	(b)			(c) 1683±12Ma(EMPA, σ?, n=?, mnz)			(e) mu-bi-gt-pl-ilm	
COL20D 46.5m				(c) 1649±12M(EMPA, σ?, n=?, mnz)			(d) gt-pl-bi-mu	
COL20D 47m	(b)			(c) 1688±13Ma (EMPA, σ?, n=?, mnz)			metapelite	
COL20D 46.6-47.5m				(a) 1690±9Ma (LA-ICP-MS,2σ, n=20,mnz)			(d) gt-bi-mu-q-pl-ilm-sill gneiss	
TAL4	(a)		(a) 1698±7Ma (2σ, n=47, z)				(a)pl-q-gt-bi-crd schist	(d) 0.53
TAL11							(b) opx-cp-pl-q	
TAL13							(b) gt-hb-bi-pl-q	
TAL20 57-57.5m	(a)			(a) 1673±9Ma (LA-ICP-MS, 2σ, n=20,mnz)			(a) q-ksp-pl-bi-sill-gt gneiss	(d) 2.39
BAC17						(d from b, p88)=108	(b) gt-hb gneiss	

Table 2: continued

Drill hole and Sample number	Whole rock geochemistry	*P–T* pseudosection	Constraints on maximum depositional age (U–Pb zircon)	Metamorphic age, monazite (mnz) or zircon (z), using EMPA (recalculated by Dutch *et al.* (2010) in (a) and LA–ICP–MS U–Pb methods	EPMA Garnet compositional traverses	Thermal gradient calculations °C/kbar	Petrographic description	Total radiogenic heat production calculations (μW m^{-3})
BAC18	(a)		(a) 1738±15Ma (2σ, n=7, z)	(a) 1696±10Ma(LA-ICP-MS, 2σ, n=17, mnz)			(a) q-bi-ksp-gt-sill-pl gneiss	(d) 4.23
BAC23	(a)	(d)	(a) 1717±11Ma (2σ, n=17, z)	(c) 1666±17Ma(EMPA, σ?, n=?, mnz) (d) 1701.2±0.8Ma (LA-ICP-MS σ2, n spots= 12 mnz)	(d)	(d) = 128 (e from b, p88) = 87.5-83	(a), (b) q-ksp-pl-bi-g-sill gneiss	(d) 3.33
BAC26							(b) gt-hb gneiss	
BAC28	(a)	(d)		(d) 1735±19Ma, (LA-ICP-MS σ=2, n=spots 9 mnz)	(d)	(d) = 130	(a) q-bi-sill-pl-gt gneiss	(d) 2.15
BAC33	(a)			(c) 1635±19Ma(EMPA, σ?, n=?, mnz)			(b) gt-sill-bi schist	(d) 3.87
BAC38						(d from b, p88) = 87.5-83	(b) gt-cpx-hb gneiss	
BAC41	(a)		(a) 1722±6Ma (2σ, n=48, z)	(a) 1664±7Ma (LA-ICP-MS, 2σ, n=30, mnz)			(d) gt-bi-sill-pl	(d) 3.01
NDR1 41m		(d)		(c) 1505±14Ma (EMPA, σ?, n=?, mnz), (d) 1599 ± 11Ma (LA–ICP–MS,, σ2, n=spots 15 mnz)	(d)	(d) =55	(b), (d) gt-bi-pl-mt-q	
NDR5 45m				(c) 1593±15Ma (EMPA, σ?, n=?, mnz)				
Nundroo Block DDH294.2m, DDH2160m (general)	(b, p91-94) RS#167			(b, p89) 1543±9Ma (SHRIMP/Kober, σ?, n=?, z)		(d from b, p88) = 87.5	(b) p91-94	

Table 2: continued

Drill hole and Sample number	Whole rock geochemistry	*P–T* pseudosection	Constraints on maximum depositional age (U–Pb zircon)	Metamorphic age, monazite (mnz) or zircon (z), using EMPA (recalculated by Dutch *et al.* (2010) in (a) and LA–ICP–MS U–Pb methods	EPMA Garnet compositional traverses	Thermal gradient calculations °C/kbar	Petrographic description	Total radiogenic heat production calculations (μW m^{-3})
Central Block (general)				(b, p90) 1672±12Ma(SHRIMP/Kober, σ?, n=?, z)			(b)	
Colona Block (general)	(b, p90) 94		(b, p92) 1730±10Ma (SHRIMP/Kober,σ?,n=?,z)				(b)	
Barton Block (general)				(b, p91) 1712±9.5Ma (SHRIMP/Kober, σ?, n=?, z)		(d from b, p88) West =114-100, East=100	(b) bi±sill±gt-kfld-q-mg±pl	

3. METHODS

3.1 Sample Preparation

Legacy samples for this study were inherited from the University of Adelaide's thin section archive. Thin sections were prepared prior to commencement of this study by Teasdale (1997). Samples were made from available drill core acquired from three drilling traverses by the former Department of Mines and Energy, South Australia (MESA) and a mineral exploration traverse (North Exploration's BAC traverse) (Figure 2; Teasdale, 1997).

3.2 LA–ICP–MS monazite U–Pb geochronology

LA–ICP–MS geochronology was performed on available monazite grains *in-situ* in thin section samples BAC23, BAC28, and NDR1. Thin sections were imaged prior to laser ablation using a backscattered electron detector on a Philips XL30 SEM (scanning electron microscope; Appendix C), in order to determine the microstructural location of monazite prior to *in-situ* ablation. U–Pb isotopic analysis were obtained using a New Wave 213 nm Nd–YAG laser in an inert He ablation atmosphere, and received by an Agilent 7500cs ICP–MS at Adelaide Microscopy, located at the University of Adelaide using the method outlined in Payne *et al.* (2008). Monazite ablation in samples was performed using a spot size of 15 µm, repetition rate of 5 Hz and a fluence of 10 J cm^{-2}, using the ATUNE acquisition software method BENmnzM. Acquisition time for each analysis was 80 s. Within this time there was 40 s of background measurement, 10 s of laser fire with shutter closed to allow for beam stabilisation, and 30 s of monazite ablation. Monazite data was processed using Glitter software (Griffin *et al.*, 2004). Mass bias and elemental fractionation was corrected using an in-house internal monazite standard 222 (SHRIMP: 206Pb/238U age 450 ± 3.4 Ma; Payne *et al.*, 2008), and primary monazite standard MADel (TIMS: 207Pb/206Pb age 492.01 ± 0.77 Ma,

206Pb/238U age 517.9 ± 2.6 Ma, 207Pb/235U age 513.13 ± 0.20 Ma; Payne *et al.*, 2008) for samples BAC23, BAC28 and NDR1. Instrument drift was corrected for with the application of a linear correction and by standard bracketing every four analyses. Weighted average ages collected throughout the course of this study for in-house monazite standard 222 were 207Pb/206Pb = 477 ± 54 Ma (n= 22, MSWD= 8.4), 206Pb/238U = 456.2 ± 6.3 Ma (n= 22, MSWD= 24), and 207Pb/235U = 466 ± 17 Ma (n= 22, MSWD= 39) and for MADel are 207Pb/206Pb = 494 ± 12 Ma (n= 39, MSWD= 10.1), 206Pb/238U = 522.5 ± 5.0 Ma (n= 39, MSWD= 5.2), and 207Pb/235U = 528 ± 13 Ma (n= 38, MSWD= 1776).

3.3 Whole rock and mineral geochemistry

This data was compiled from previous work performed by Howard *et al.* (2011a) and Mining and Energy South Australia (MESA) in Teasdale (1997). Methods for whole rock geochemical analysis can be found in Howard *et al.* (2011b), for samples BAC23 and BAC28. For sample NDR1 geochemistry was performed by Mines and Energy South Australia (MESA) and compiled by Teasdale (1997). X-ray maps and chemical analyses of minerals were acquired via Cameca SX5 electron microprobe analysis (EPMA) at Adelaide Microscopy, University of Adelaide. Point analysis used a beam current of 20 nA, accelerating voltage of 15 kV, and a defocussed beam size of 5 µm, and a PAP correction was applied to all data. Analyses were made for SiO_2, TiO_2, Cr_2O_3, Al_2O_3, FeO, MnO, MgO, CaO, Na_2O, K_2O, ZnO and P_2O_5 on Wavelength Dispersive Spectrometers (WDS). Calibration was done on natural and synthetic mineral standards supplied by Astimex, Taylor and P&H. For elemental x-ray maps of garnet grains a 15 kV accelerating voltage, a beam current of 150 nA, a dwell time of 50 ms and a step size of 20 µm was used. Fe, Mg, Mn, Ca, Al, Ce, Cl, F, K, Na, Si, Ti and Zr were analysed on WDS and Electron Dispersive Spectrometers.

3.4 Phase equilibria forward modelling

Phase equilibria calculations were performed using the software programs THERMOCALC and Perple_X (Powell and Holland, 1998; Connolly and Petrini, 2002; Connolly, 2005; Holland and Powell, 2011) in the chemical system MnO–Na_2O–CaO–K_2O–FeO–MgO–Al_2O_3–SiO_2–H_2O–TiO_2–O, where 'O' is a proxy for Fe2O3, using the latest internally-consistent thermodynamic dataset 'ds6' (filename tc-ds62.txt; Holland and Powell (2011)) and activity–composition models (Powell *et al.*, 2014; White *et al.*, 2014b).

Calculations in THERMOCALC are based on the user specifying the stable assemblage and calculating the diagram line by line, point by point, where lines (field boundaries) represent the zero abundance of a phase and points represent the zero abundance of two phases. The initial stable assemblage is determined by performing a Gibbs energy minimisation calculation at a set pressure–temperature (*P*–*T*) condition. The diagram is built up and around from that initial assemblage and involves many trial and error calculations in order to determine which phases appear or disappear as a function of pressure, temperature and/or composition. In addition, the so-called 'starting guesses' (values for variables with which THERMOCALC commences its iterative least-squares calculation for a line or point) require regular updating as the pseudosection is calculated in different parts of *P*–*T*–*X* space (*X* = composition). Therefore, a single diagram commonly comprises >150–200 total line and point calculations, and the user is actively (intellectually), rather than passively, involved in the calculations at every step along the way (this amounts to a considerable amount—up to several weeks—per diagram). The most uncertain compositional variables are Fe2O3 and H2O, commonly requiring that these be constrained with *T*–*M* type diagrams (where M refers to amount) prior to the calculation of the pressure–temperature (*P*–*T*) pseudosection. The choice of pressure at which to calculate the T–M diagrams is based on broadly estimating the pressure where the petrographically-determined peak metamorphic assemblage is stable.

Calculations in Perple_X are based on Gibbs energy minimisation over a user-specified gridded *P–T* or *T–X* range. The calculation of pseudosections in Perple_X is automated such that the user only need specify the rock ('bulk') composition, the list of solid-solution phases to be used by the calculation process and the *P–T* range. Some pseudosections have been calculated in Perple_X (*T–*M_O: BAC28, NDR1; *T–*M_{H2O}: BAC23, BAC28, NDR1; *P–T*: BAC23, BAC28, NDR1) for the sake of time constraints, but it is by using THERMOCALC that the skill set of learning phase equilibria is developed.

3.5 Apparent thermal gradient calculations

Peak *P–T* conditions were constrained from calculated *P–T* pseudosections for three samples from the Fowler Domain, two from the Barton Block and one from the Nundroo Block. Peak *P–T* conditions were determined on the basis of locating mineral assemblages interpreted from petrographic analysis in fields on *P–T* pseudosections, and where possible, by additionally coupling calculated with measured mineral chemistry (garnet chemistry, CaO/(CaO+MnO+FeO+MgO)) inside the peak assemblage field. Apparent thermal gradient calculations were performed by dividing peak temperature (°C) by pressure (kilobar; at the peak temperature), *T*/*P*.

4. RESULTS

4.1 Metamorphic petrography

Thin sections of the Barton and Nundroo Block metasediments, from drill holes BAC23, BAC28 and NDR1 (Figure 2) were used for petrography, geochronology and *P–T* analysis. Peak and retrograde mineral assemblages have been interpreted on the basis of microstructural relationships and grain size.

4.1.1 Barton Block metasediments

Samples BAC23 and BAC28

These samples contain quartz, potassium feldspar, plagioclase, biotite, garnet, sillimanite, ilmenite and magnetite. BAC23 does not contain potassium feldspar but the relationship between other minerals remains the same. Porphyroblasts of garnet (2–5 mm) are sub-angular. These grains variably and exclusively contain poikiloblasts of angular to sub-rounded biotite, angular to sub-rounded ilmenite, quartz and magnetite to a lesser extent. Ilmenite, magnetite (small amounts) and quartz are also adjacent (external) to garnet and all other minerals are external to garnet (Figure 3). Garnet rims are in contact with elongate biotite and ilmenite, and rarely with sillimanite. Coarse grained biotite (5–10 mm long) and sillimanite (2–8 mm long) surround garnet and define the foliation along with variably elongated grains of ilmenite (2–4 mm) and tabular quartz, sillimanite, plagioclase and (in BAC28) potassium feldspar. Oriented and tabular sillimanite commonly occurs proximal to garnet, however only rarely makes direct contact and is seen to occur more commonly with adjacent biotite and ilmenite. Potassium feldspar in BAC28 is rounded to sub-rounded, coarse grained (2–5 mm) and common compared to minor fine-grained plagioclase (<1 mm). Potassium feldspar grains are in direct contact with sillimanite, biotite and ilmenite and sometimes contain inclusions of biotite and ilmenite. Sub-angular plagioclase is coarse grained in BAC23 (2–5 mm), occurring throughout the sample distal to garnet and proximal to biotite and sillimanite. Plagioclase is comparatively fine grained in BAC28 (1–<0.5mm) and less common, occurring within elongate ilmenite and magnetite. The peak metamorphic mineral assemblage for these two samples is interpreted to be garnet + sillimanite + biotite + quartz + plagioclase + ilmenite ± magnetite, with additional potassium feldspar in BAC28.

4.1.2 Nundroo Block metasediments

Sample NDR1

This sample contains garnet, biotite, plagioclase, potassium feldspar, ilmenite and quartz. Coarse-grained garnet (2–5 mm) porphyroblasts are euhedral to sub-rounded. Poikiloblastic garnet consist of elongate to sub-rounded biotite, ilmenite and quartz exclusively, and these same minerals also occur in fractures in garnet. Garnet tends to be mantled by biotite, which also defines foliation. However, garnet grains are also variably in contact with plagioclase, ilmenite and quartz. Abundant medium to coarse-grained (1–5 mm) plagioclase also contains inclusions of ilmenite and biotite. Potassium feldspar occurs to a lesser extent in this sample than in the Barton Block samples, it is finer grained (1– <1mm) and sparsely distributed throughout. The peak metamorphic mineral assemblage for this sample is interpreted to be garnet + biotite + plagioclase + ilmenite + quartz ± potassium feldspar.

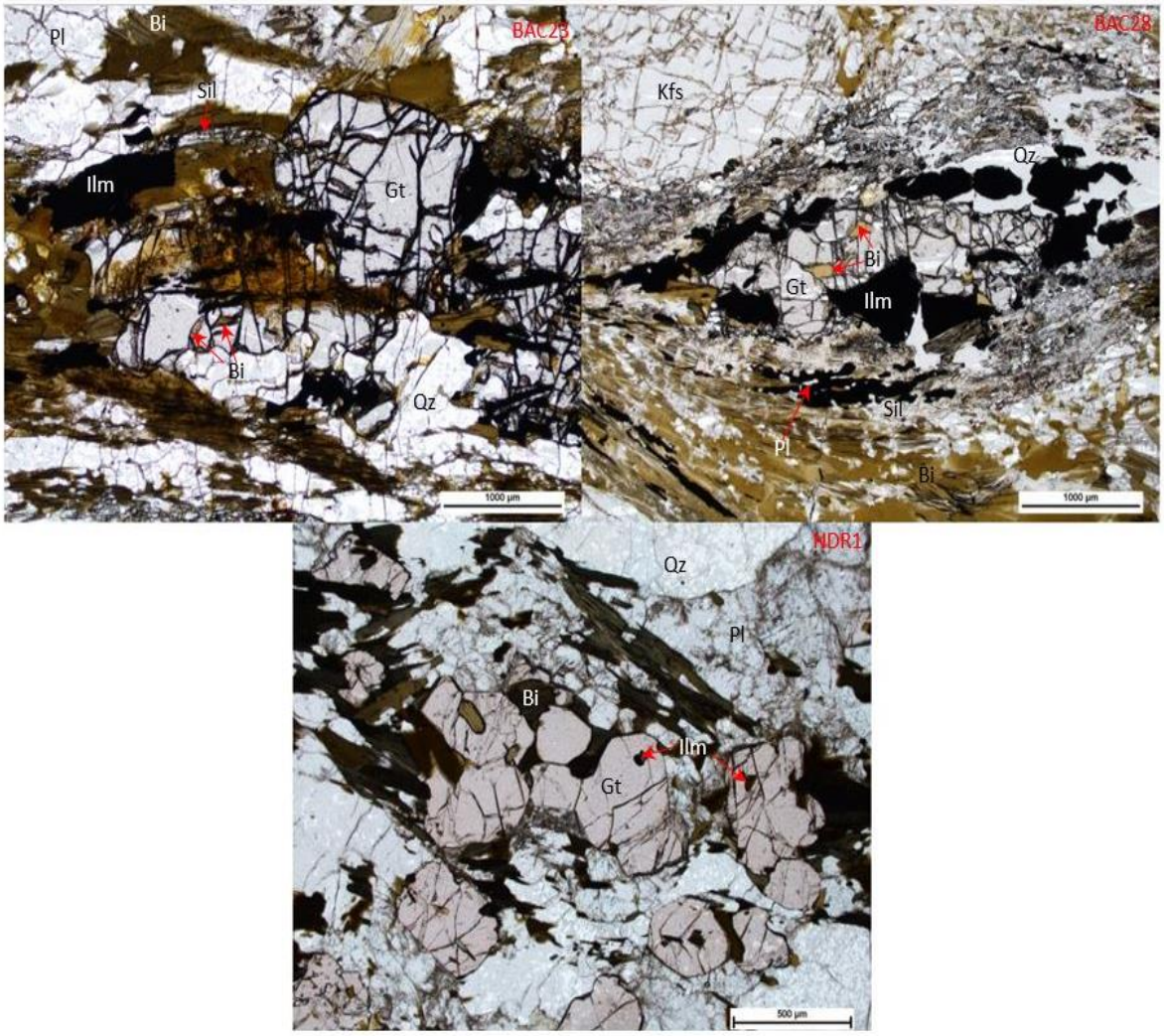

Figure 3. Photomicrographs of petrological relationships. Barton Block sample BAC23 and BAC28: garnet grains contain inclusions of biotite, ilmenite and quartz. These minerals are also adjacent to garnet, all other minerals, e.g. sillimanite, remain external to garnet. BAC28 only: coarse grained biotite and sillimanite surround garnet and define foliation as well as variably elongated grains of ilmenite and tabular quartz, sillimanite, potassium feldspar and ilmenite. Garnet rims are in contact with biotite and ilmenite, and rarely with sillimanite. Nundroo Block sample NDR1: sub-euhedral garnet with biotite and ilmenite inclusions, plagioclase and quartz are external to garnet and occasionally in contact with garnet rims, biotite external to garnet grains define foliation.

4.2 LA–ICP–MS monazite U–Pb Geochronology

LA–ICP–MS U–Pb analysis was performed *in-situ* on monazite in three thin section samples; two from the Barton Block (BAC23, BAC28) and one from the Nundroo Block (NDR1).

Sample BAC23

20 analyses were obtained from 18 individual monazite grains. Of the 20 analyses, 4 were rejected due to a high concentration of ^{204}Pb, and an additional 4 were excluded from age calculations (>5% concordance). The data records an age spread from 1705–1820 Ma, with a weighted average age of 1701 ± 8.0 Ma (*n*=12, MSWD=1.5, Figure 4a).

Sample BAC28

20 analyses were obtained from 15 individual monazite grains. Of the 20 analyses, 5 were rejected due to a high concentration of ^{204}Pb, and an additional 6 were excluded from age calculations (>5% concordance). The data records an age spread from 1719–1811 Ma, with a weighted average age of 1735 ± 19 Ma (*n*=9, MSWD=2.7, Figure 4b).

Sample NDR1

23 analyses were obtained from 10 individual monazite grains. Of the 23 analyses, 5 were rejected due to a high concentration of ^{204}Pb, and an additional 5 were excluded from age calculations (>5% concordance). The data records an age spread from 1570–1672 Ma, with a weighted average age of 1599 ± 11Ma (*n*=15, MSWD=1.9, Figure 4c).

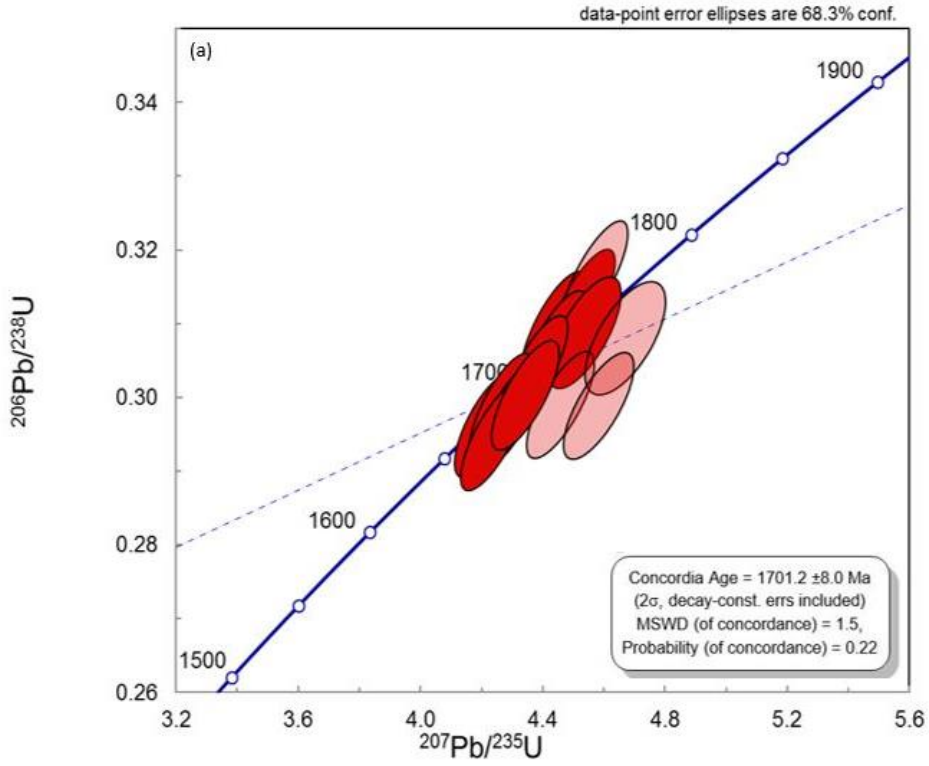
data-point error ellipses are 68.3% conf.
(a)
1900
1800
1700
1600
1500
Concordia Age = 1701.2 ±8.0 Ma
(2σ, decay-const. errs included)
MSWD (of concordance) = 1.5,
Probability (of concordance) = 0.22
0.34
0.32
0.30
0.28
0.26
3.2
3.6
4.0
4.4
4.8
5.2
5.6
206Pb/238U
207Pb/235U

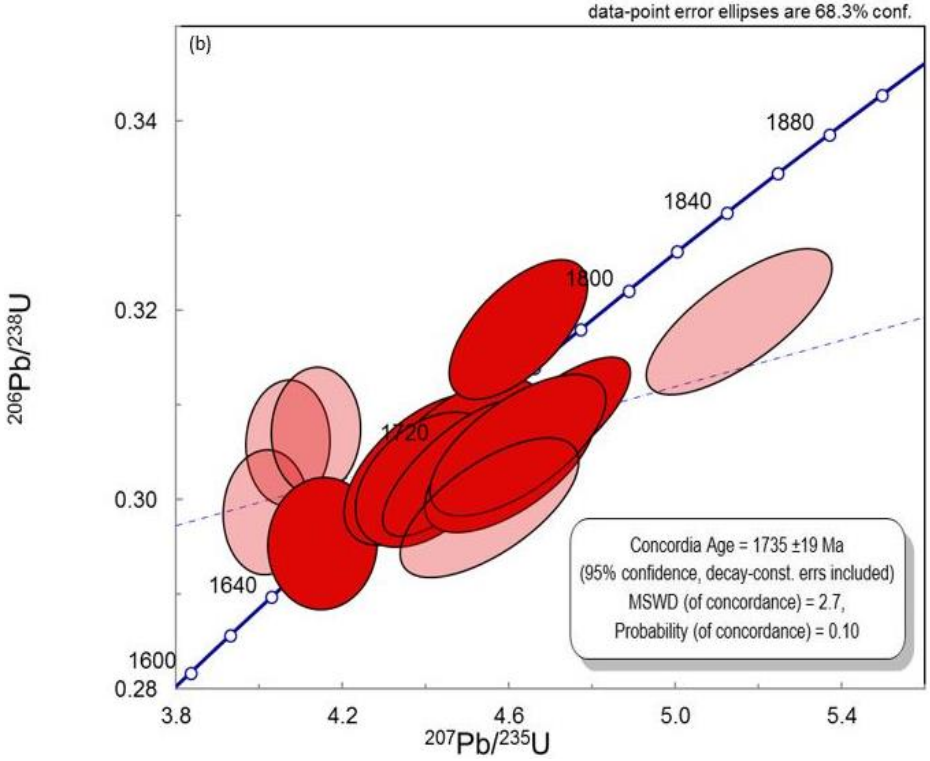
data-point error ellipses are 68.3% conf.
(b)
1880
1840
1800
1720
1640
1600
Concordia Age = 1735 ±19 Ma
(95% confidence, decay-const. errs included)
MSWD (of concordance) = 2.7,
Probability (of concordance) = 0.10
0.34
0.32
0.30
0.28
3.8
4.2
4.6
5.0
5.4
206Pb/238U
207Pb/235U

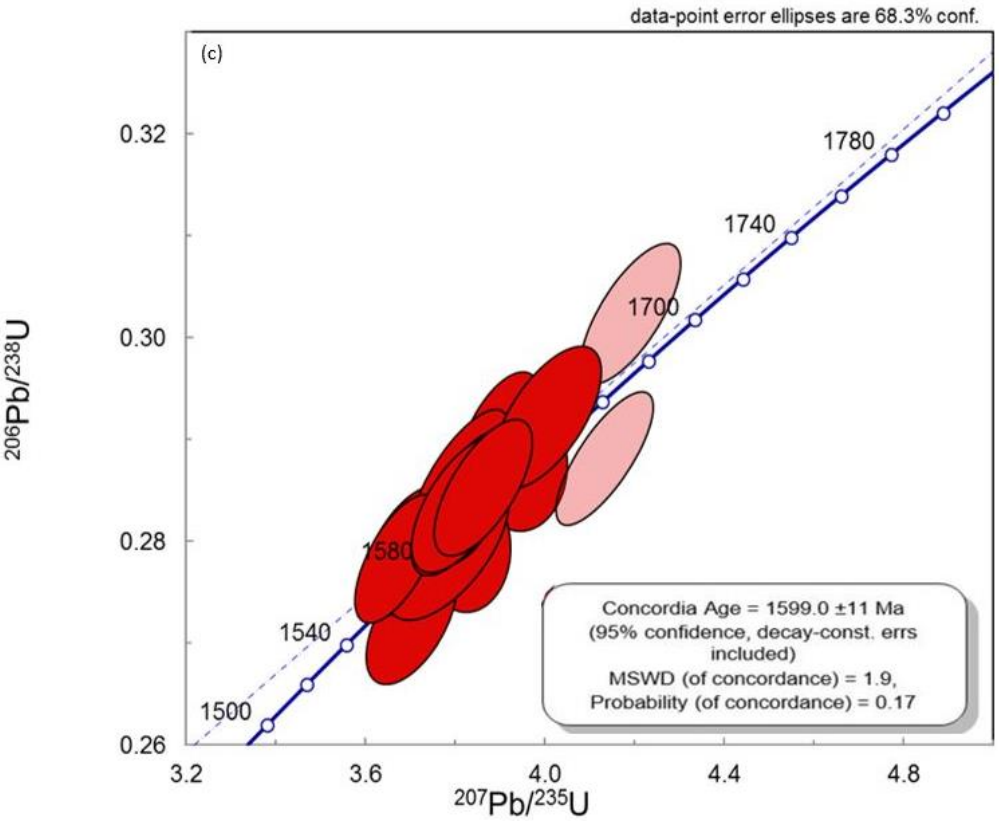

Figure 4. U-Pb LA-ICP-MS analysis Concordia plots for (a) BAC23, (b) BAC28 and (c) NDR1. Analyses which are > 10% discordant are light pink for clarity.

4.3 Mineral geochemistry

Whole rock geochemical analysis for NDR1 can be found in Teasdale (1997), and for BAC23, BAC28 in Howard *et al.* (2011b). Mineral geochemistry is summarised in Table 3 and full analyses of each mineral and elemental maps are given in Appendix A. Garnet traverses for each sample are discussed below.

Table 3. Chemical ranges of selected minerals from EPMA analysis.

	BAC23	BAC28	NDR1
Garnet core			
X_{alm}	0.789 - 0.367	0.263 - 0.224	0.549 - -0.670
X_{py}	0.460 - 0.049	0.322 - 0.250	0.928 - 0.180
X_{grs}	0.087 - 0.021	0.0639 - 0.051	0.166 - 0.000
X_{sps}	0.145 - 0.059	0.406 - 0.346	0.073 - 0.000
Garnet rim			
X_{alm}	0.994 - 0.382	0.260 - 0.220	0.544 - 0.523
X_{py}	0.476 - 0.005	0.308 - 0.261	0.274 - 0.206
X_{grs}	0.054 - 0.001	0.063 - 0.056	0.144 - 0.093
X_{sps}	0.080 - 0.000	0.390 - 0.369	0.073 - 0.068
Biotite			
Al2O3 (wt%)	17.901 - 15.917	26.433 - 17.988	16.236 - 15.047
MnO (wt%)	0.052 -0.018	0.371 - 0.145	0.058 - 0.023
TiO2 (wt%)	2.371 - 1.728	2.120 - 1.289	4.571 - 2.863
Cl (wt%)	0.053 -0.003	0.015 - 0.000	0.018 - 0.002
X_{Fe}	0.208 -0.178	0.203 - 0.103	0.377 - 0.331
K-feldspar			
X_{or}	-	0.981 - 0.183	0.018 - 0.012
Plagioclase			
X_{ab}	-	-	0.428 - 0.330
Ilmenite			
TiO2 (wt%)	11.452 - 6.859	36.675 - 6.727	
MnO (wt%)	0.008 -0.000	0.156 - 0.065	
Magnetite			
TiO2 (wt%)	-	-	0.693 - 0.660
Al2O3 (wt%)	-	-	0.544 - 0.278

X_{alm} = Fe2+/(Fe2+ + Mg + Ca + Mn), X_{py} = Mg/(Fe2+ + Mg + Ca + Mn), X_{grs} = Ca/(Fe2+ + Mg + Ca + Mn), X_{sps} = Mn/(Fe2+ + Mg + Ca + Mn), Xfe = Fe/(Fe2+ + Mg), X_{or} = K/(K+Na+Ca), X_{ab} = Na/(Na + Ca)

Garnet mineral compositions (of elements Fe, Mg, Ca and Mn) are expressed as mole fractions, X, (abbreviations as above, mole fraction x 100 = mole %) recalculated from electron microprobe analyses (see Appendix A)

4.3.1 Barton Block metapelites

Compositional traverses across two garnet grains in sample BAC23 and two garnet grains in sample BAC28 show different zoning trends (Figures 5 and 6). The traverses across garnet in sample BAC23 display a slight increase from rim to core in X_{alm} (= Fe^{2+}/(Mg + Fe^{2+} + Ca + Mn) cations), with values of 0.39 at the rim where it is contact with biotite, to 0.79 at the core, whereas sample BAC28 shows little change in X_{alm} with values at ~0.25. X_{py} (= Mg/(Mg + Fe^{2+} + Ca + Mn) cations) values in BAC23

are relatively stable and increase slightly from rim to core, and range from 0.48 to 0.45, respectively. In sample BAC28 X_{py} values show an increase from rim (0.25) to core (0.35). X_{grs} (= Ca/(Mg + Fe^{2+} + Ca + Mn) cation) values in BAC23 are constant with values of ~0.05 across garnet. X_{grs} increases slightly from garnet core to rim in BAC28 with respective values of 0.049 to 0.063. X_{sps} (= Mn/(Mg + Fe^{2+} + Ca + Mn) cations) in BAC23 increase steeply from rim to core with values of 0.08 (rim) to 0.145 (core). Values of X_{sps} in BAC28 are high throughout the traverse but increase slightly towards the rim (0.430), and decrease at the core (0.345). The elemental maps of garnet grains in BAC23 (Figure 5) and BAC28 (Figure 6) reflect these trends. Figure 5 shows Fe increasing sharply from rim to core and Mn increasing gradually from core to rim, whereas Mg increases from rim to core and Ca remains relatively constant across the grain. Figure 6 displays Fe concentrations remaining essentially constant across the garnet grain, whereas Mg shows a gradual increase from rim to core. It is difficult to see the subtle increase of Ca from core to rim in BAC28, and the Mn map shows an increase in elemental concentrations from core to rim (Figure 6).

4.3.2 Nundroo Block metapelite

Compositional traverses across two garnet grains in sample NDR1 show different zoning patterns (Figure 7) to those from the Barton Block. X_{alm} values increase from rim (proximal to biotite) to core with values of 0.342 and 0.552, respectively. Values for X_{py} decrease from rim (0.648) to core (0.235), and X_{grs} values dramatically decrease from rim (0.141) where garnet is in contact with plagioclase, to core (0.074). The values for X_{sps} remain constant across the grains with values of ~0.07 (Figure 7). Elemental maps (Figure 7) supports the above analyses where Fe and Mg concentrations increase towards the core of the garnet. The Ca portion in Figure 7 shows the most significant zoning pattern of all the maps. The dramatic increase in Ca towards the rim when garnet is in contact with plagioclase is clearly visible.

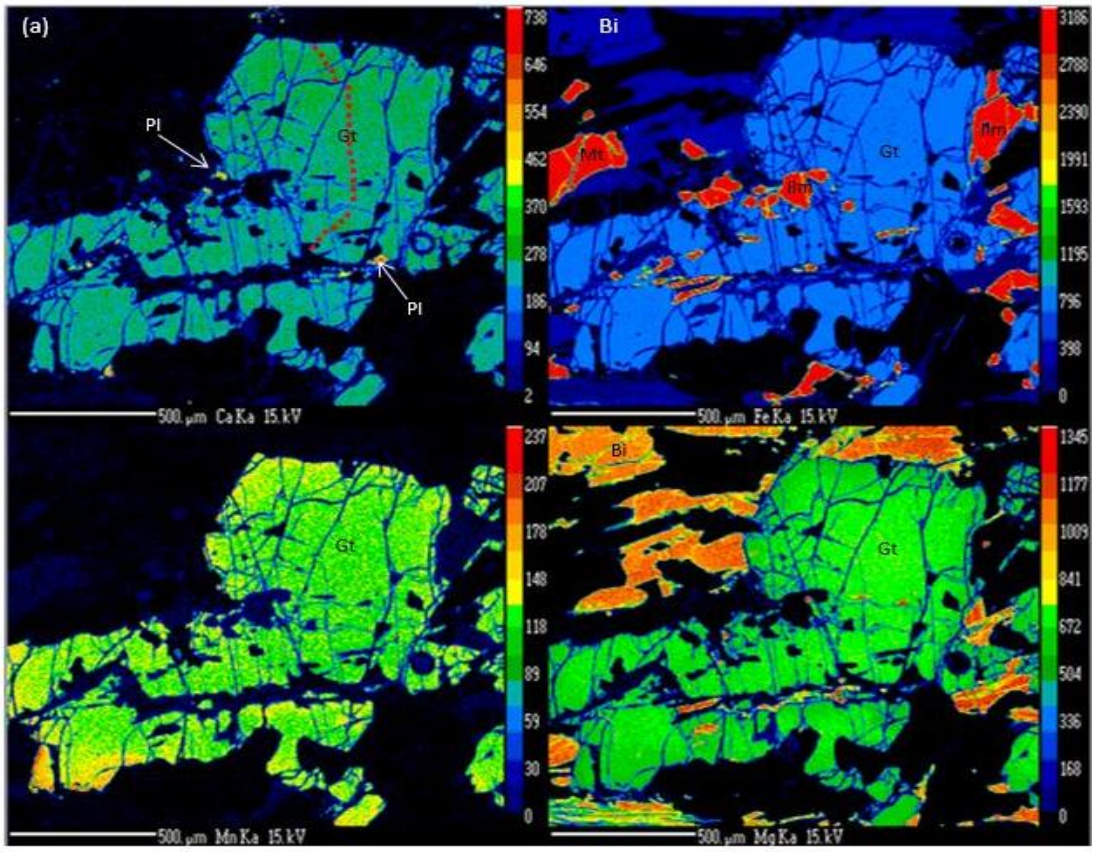

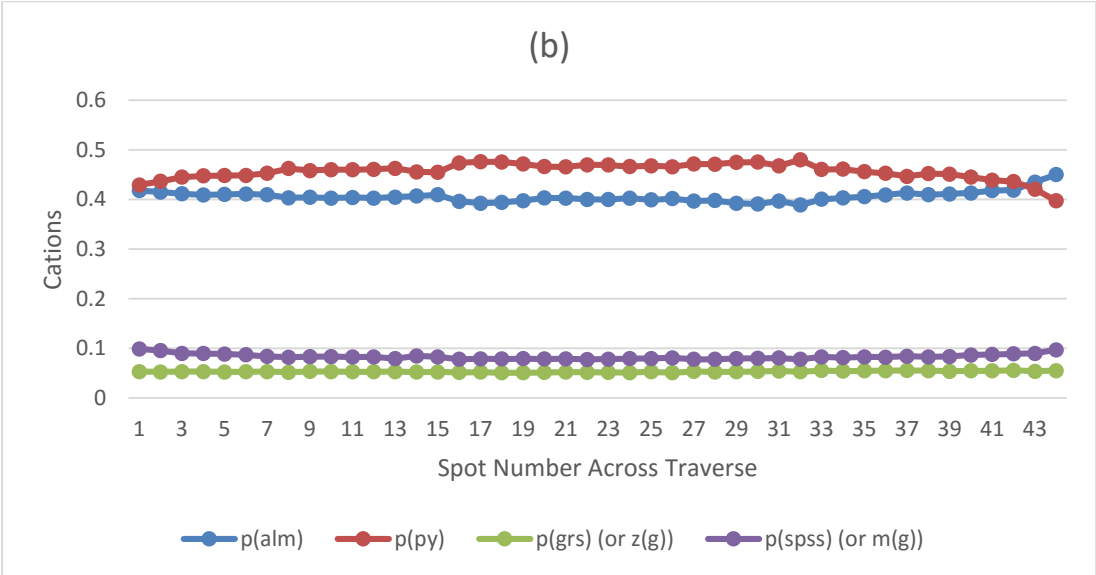

Figure 5. (a) EPMA elemental maps Ca, Fe, Mn, and Mg from sample BAC23. Zero concentration is shown as black. Low concentrations are denoted by blue colouring and higher concentrations trend towards warmer colours (i.e. red) (note different scales on the Y axis of each map). (b) Compositional traverses across garnet that reveal zoning in Fe, Mg, Ca, Mn. Abbreviations below the plot represent proportions of garnet end-members: alm= almandine, Fe; py = pyrope, Mh; grs = grossular, Ca; and spss = spessartine, Mn. Red dotted line on Ca image in (a) indicates location of compositional traverse.

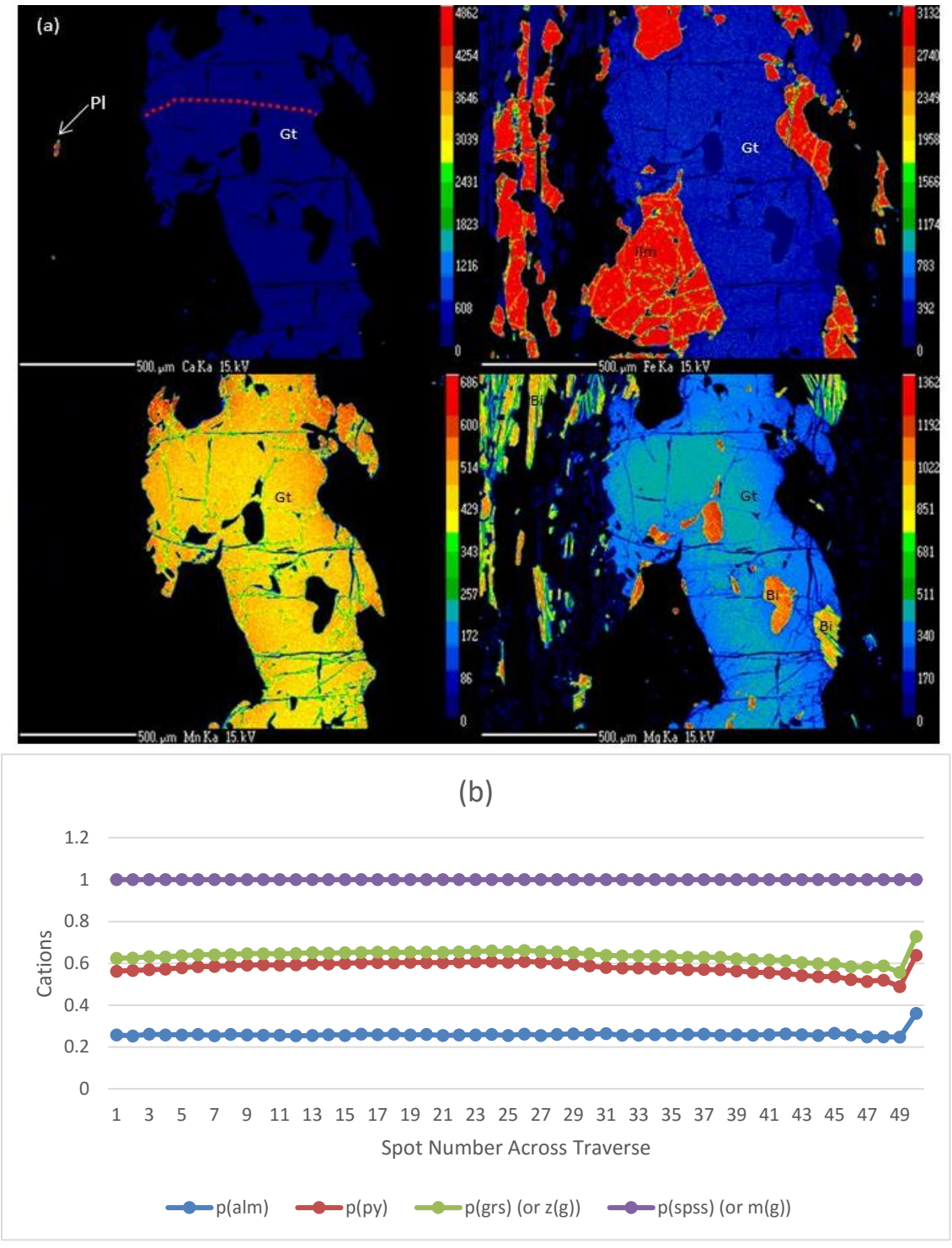

Figure 6. (a) EPMA elemental maps Ca, Fe, Mn, and Mg from sample BAC28. Zero concentration is shown as black. Low concentrations are denoted by blue colouring and higher concentrations trend towards warmer colours (i.e. red) (note different scales on the Y axis of each map). (b) Compositional traverses across garnet that reveal zoning in Fe, Mg, Ca, Mn. Abbreviations below the plot represent proportions of garnet end-members: alm= almandine, Fe; py = pyrope, Mh; grs = grossular, Ca; and spss = spessartine, Mn. Red dotted line on Ca image in (a) indicates location of compositional traverse.

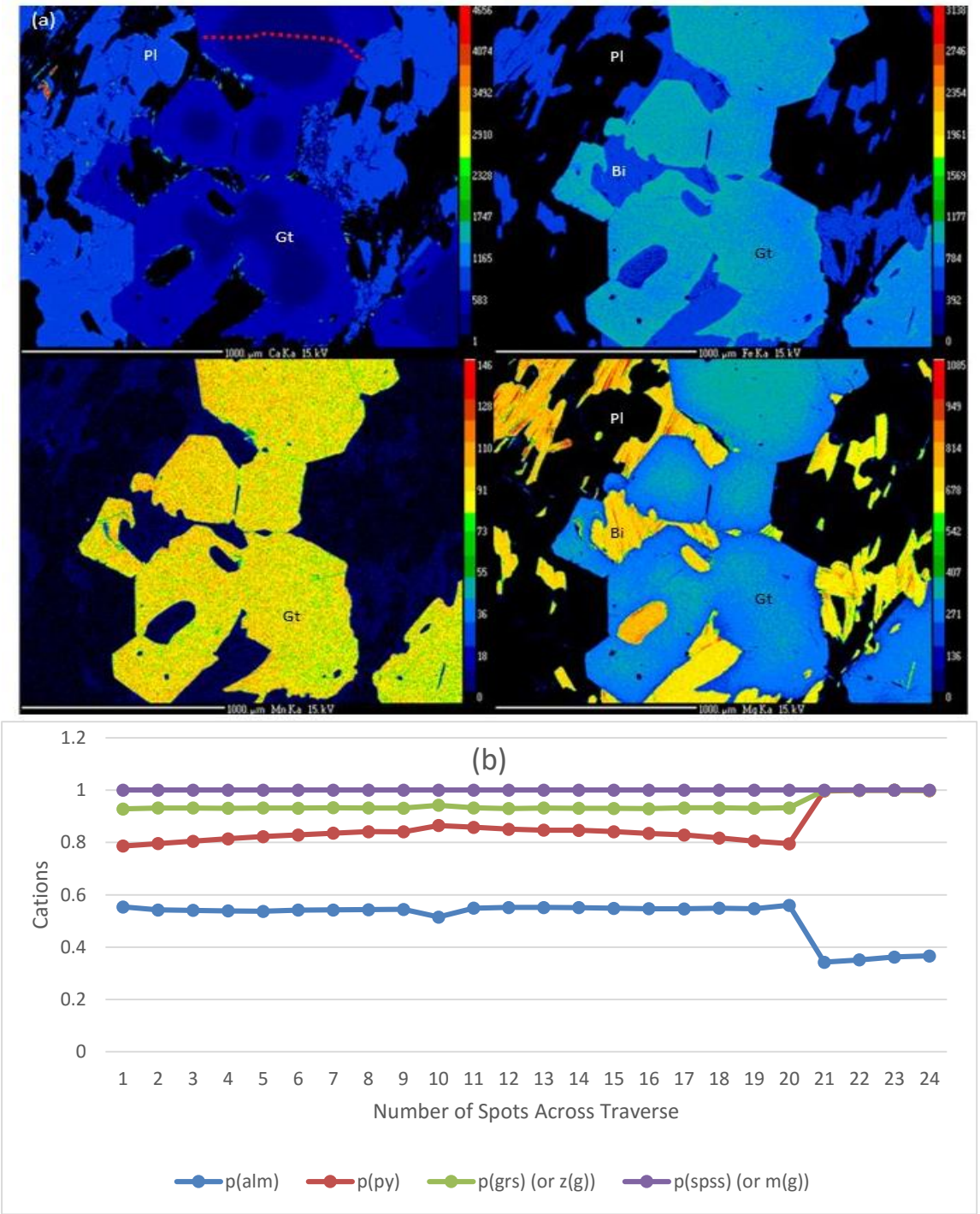

Figure 7. (a) EPMA elemental maps Ca, Fe, Mn, and Mg from sample NDR1. Zero concentration is shown as black. Low concentrations are denoted by blue colouring and higher concentrations trend towards warmer colours (i.e. red) (note different scales on the Y axis of each map). (b) Compositional traverses across garnet that reveal zoning in Fe, Mg, Ca, Mn. Abbreviations below the plot represent proportions of garnet end-members: alm= almandine, Fe; py = pyrope, Mh; grs = grossular, Ca; and spss = spessartine, Mn. Red dotted line on Ca image in (a) indicates location of compositional traverse.

4.4 Phase equilibria modelling

The objective of the phase equilibria modelling is to constrain *P–T* conditions for a number of samples in order to characterize the thermal regime causing metamorphism. The principle uncertainty in pseudosection modelling relates to the determination of the effective bulk composition, particularly Fe_2O_3 and H_2O (Korhonen *et al.*, 2012; Kelsey and Hand, 2015; Morrissey *et al.*, 2015). Therefore the appropriate O and H_2O contents for the *P–T* pseudosections were constrained for each sample by calculating, in order, $T–M_O$ and $T–M_{H2O}$ pseudosections. In each $T–M_O$ section the oxidation state along the *M* axis varies from 0% Fe_2O_3, 100% FeO at *M* = 0 to 66% Fe_2O_3, 34% FeO at *M* = 1. In each $T–M_{H2O}$ section the amount of water varies from 0.01 (or 0.001) wt% at *M* = 0 to the analysed LOI amount at *M* = 1. The fixed pressure for the $T–M_O$ and $T–M_{H2O}$ sections was chosen to be 5 kbar for all three samples on the basis of the silicate mineral assemblage (eg. White *et al.*, 2014a)

4.4.1 $T–M_O$ pseudosections

$T–M_O$ pseudosections were calculated for three metapelites BAC23 (Figure 8), BAC28 (Figure 9) and NDR1 (Figure 10). The amount of 'O' (proxy for Fe_2O_3) and thus the oxidation state of the rock composition chosen to be appropriate for the next ($T–M_{H2O}$) diagrams was based on the identification of the field containing the peak mineral assemblage (interpreted from petrography) in the $T–M_O$ diagram. A coloured vertical line (i.e. constant composition) in each of Figures 8–10 denotes the rock composition used for subsequent phase diagrams. The chosen compositions in terms of oxidation state (M_O) are 0.40 for BAC23, 0.40 for BAC28 and 0.50 for NDR1.

	H2O	SiO2	Al2O3	CaO	MgO	FeO	K2O	Na2O	TiO2	MnO	O
Mo = 0:	8.160	68.230	10.080	0.180	3.350	6.560	2.350	0.400	0.640	0.050	0
Mo = 1:	7.99	66.81	9.87	0.17	3.28	6.38	2.30	0.39	0.62	0.05	2.13

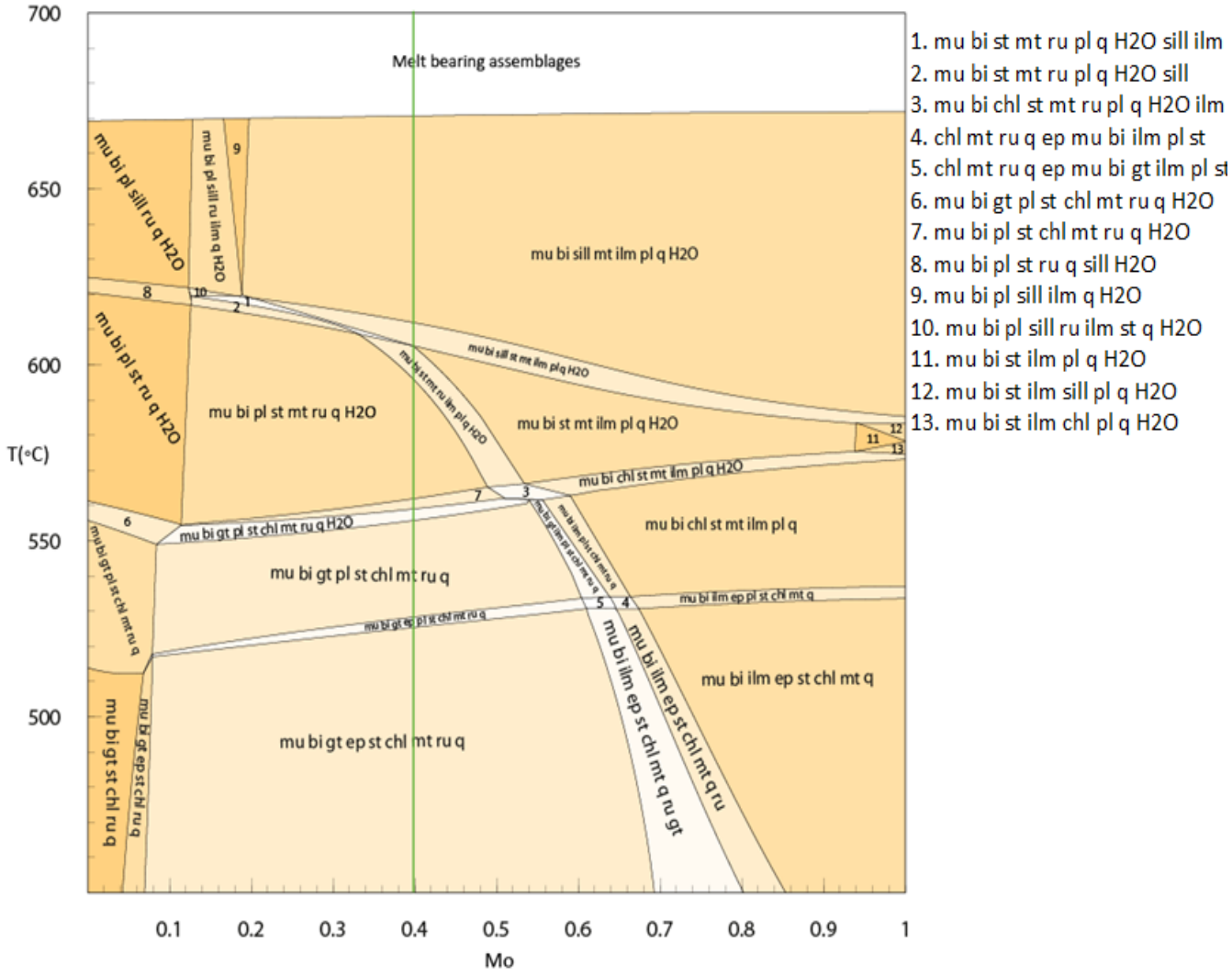

Figure 8. *T*–M_O pseudosection for sample BAC23 calculated at 5 kbar. Bulk compositions in mole% oxide provided above the diagram are: top row is for M_O = 0 (left-hand side of diagram) and bottom row is for M_O = 1.0 (right-hand side of diagram). Vertical green line indicates bulk composition used for subsequent *T*–M_{H2O} and *P*–*T* pseudosections. Fields that are too small for a legible label are numbered and the corresponding assemblage is listed to the right of the diagram.

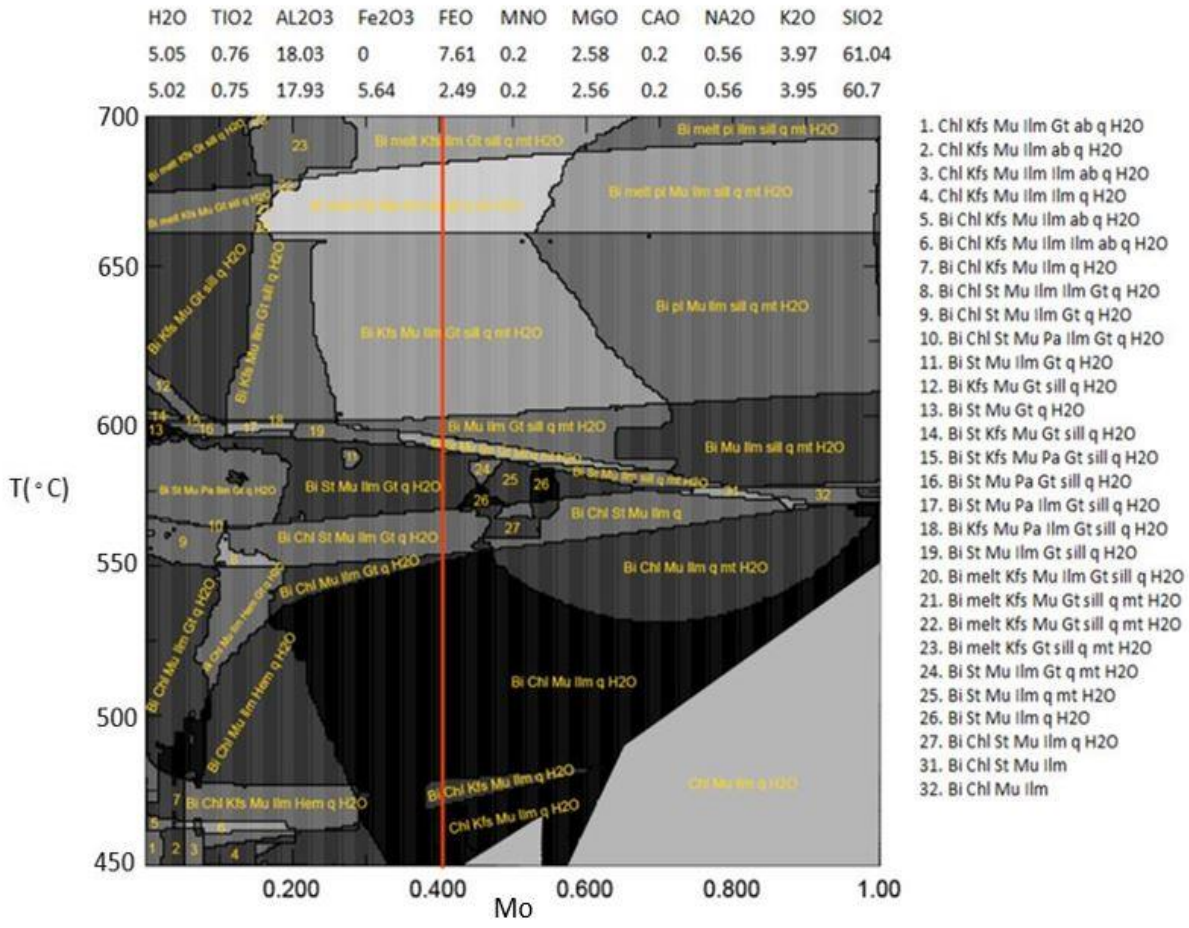

Figure 9. *T–M*$_O$ pseudosection for sample BAC28 calculated at 5 kbar. Bulk compositions in wt% oxide provided above the diagram are: top row is for *M*$_O$ = 0 (left-hand side of diagram) and bottom row is for *M*$_O$ = 1.0 (right-hand side of diagram). Vertical red line indicates bulk composition used for subsequent *T–M*$_{H2O}$ and *P–T* pseudosections. Fields that are too small for a legible label are numbered and the corresponding assemblage is listed to the right of the diagram.

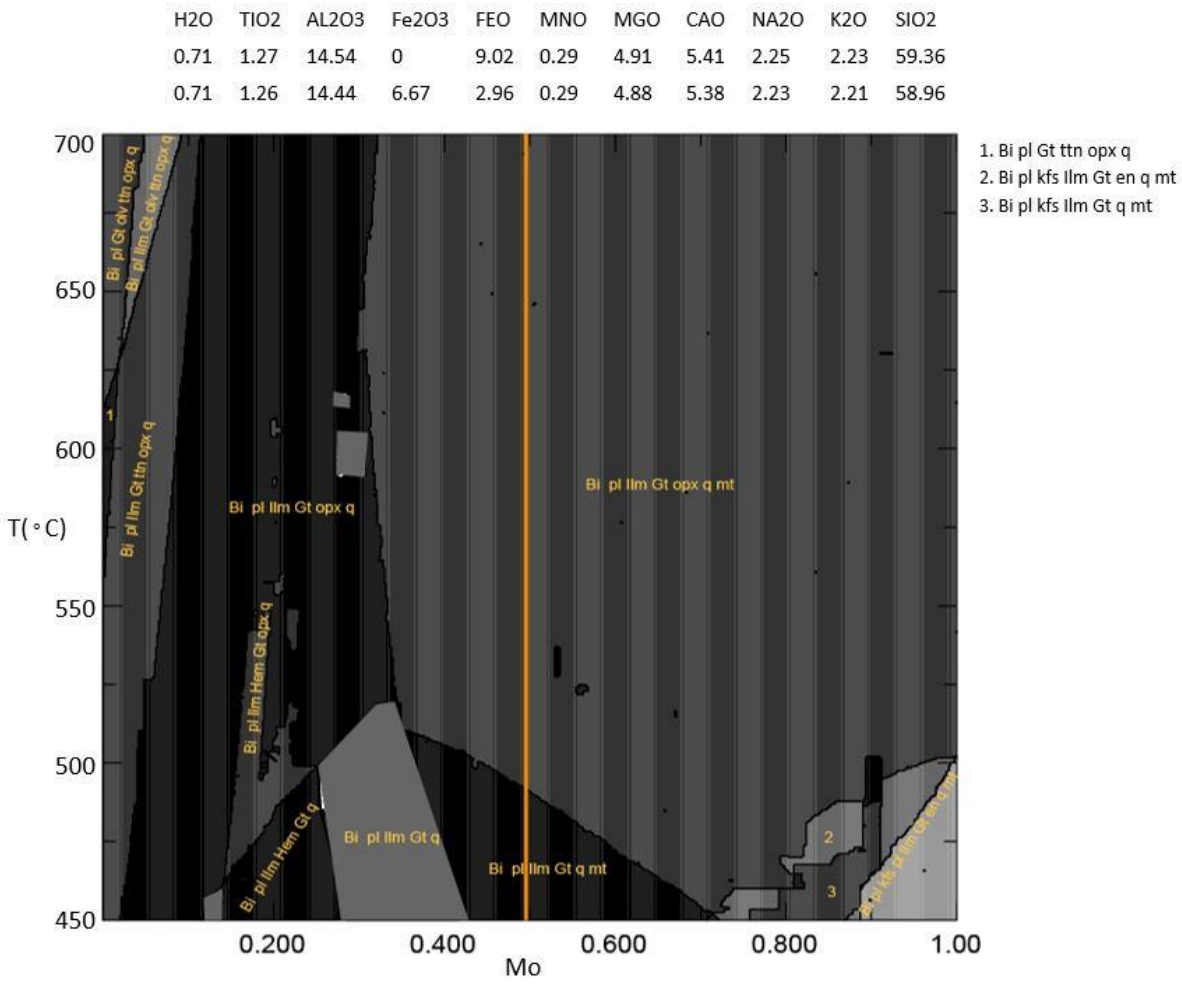

Figure 10. *T*–M_O pseudosection for sample NDR1 calculated at 5 kbar. Bulk compositions in wt% oxide provided above the diagram are: top row is for M_O = 0 (left-hand side of diagram) and bottom row is for M_O = 1.0 (right-hand side of diagram). Vertical orange line indicates bulk composition used for subsequent *T*–M_{H2O} and *P*–*T* pseudosections. Fields that are too small for a legible label are numbered and the corresponding assemblage is listed to the right of the diagram.

4.4.2 *T*–M_{H2O} pseudosections

T–M_{H2O} pseudosections were calculated for three metapelite samples BAC23 (Figure 11), BAC28 (Figure 12) and NDR1 (Figure 13) based on the composition constrained by the *T*–M_O modelling. Choice of the amount of H_2O in the rock composition was chosen based on: 1. locating the peak mineral assemblage (from petrographic observations) field in the diagram; 2. taking into account the

abundance of phases observed in thin section, especially the hydrous phases biotite and muscovite. A vertical coloured line in each of Figures 11–13 denotes the composition chosen for the next stage, the *P–T* pseudosections. The chosen compositions in terms of H_2O amount (M_{H2O}) are 0.22 for BAC23, 0.02 for BAC28 and 0.98 for NDR1.

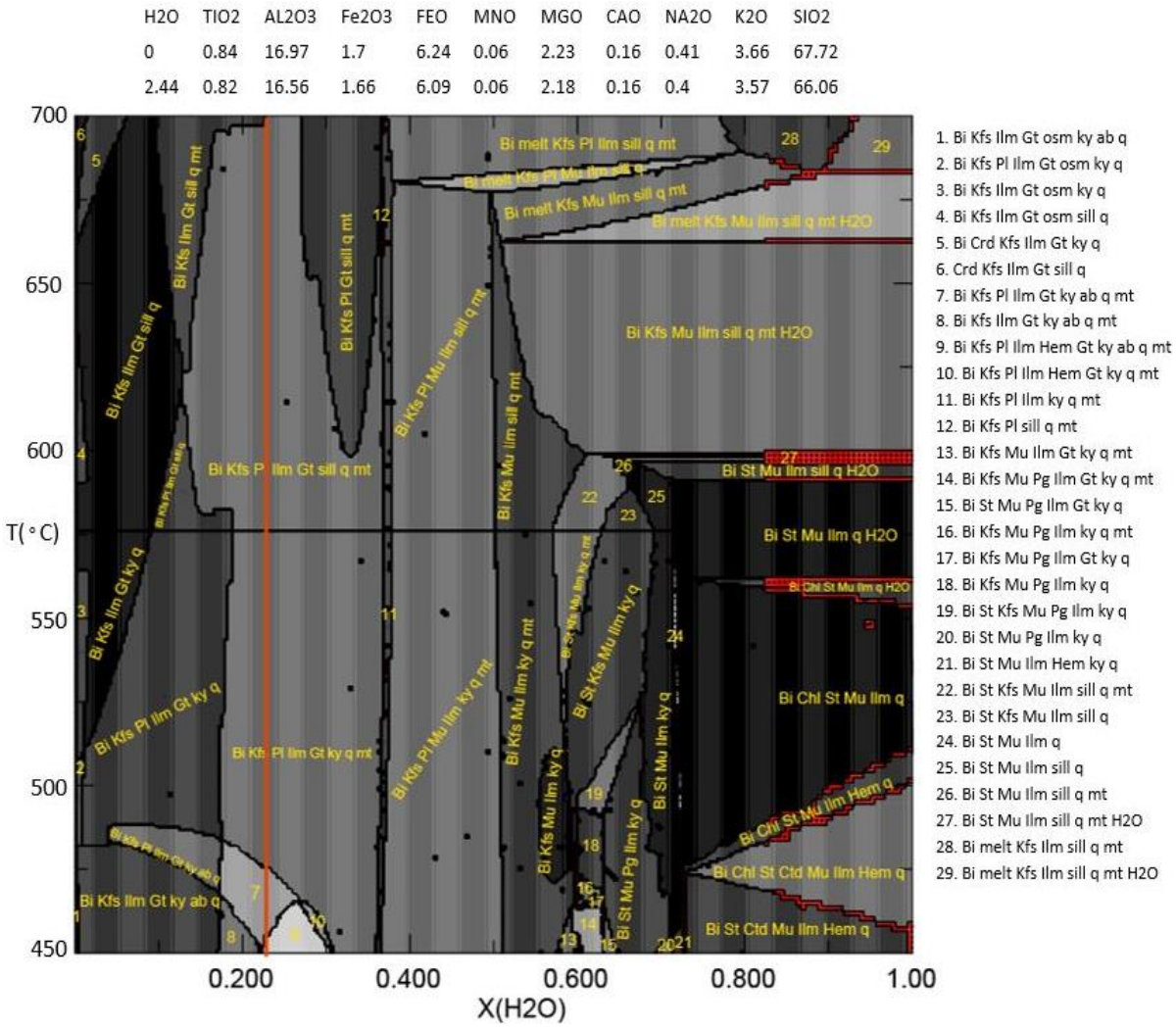

Figure 11. *T–M*$_{H2O}$ pseudosection for sample BAC23 calculated at 5 kbar. Bulk compositions in wt% oxide provided above the diagram are: top row is for M_{H2O} = 0 (left-hand side of diagram) and bottom row is for M_{H2O} = 1.0 (right-hand side of diagram). Vertical red line indicates bulk composition used for the subsequent *P–T* pseudosection. Fields that are too small for a legible label are numbered and the corresponding assemblage is listed to the right of the diagram. The red field or field boundary highlights at the right hand side of the diagram were produced by Perple_X and do not carry any significance.

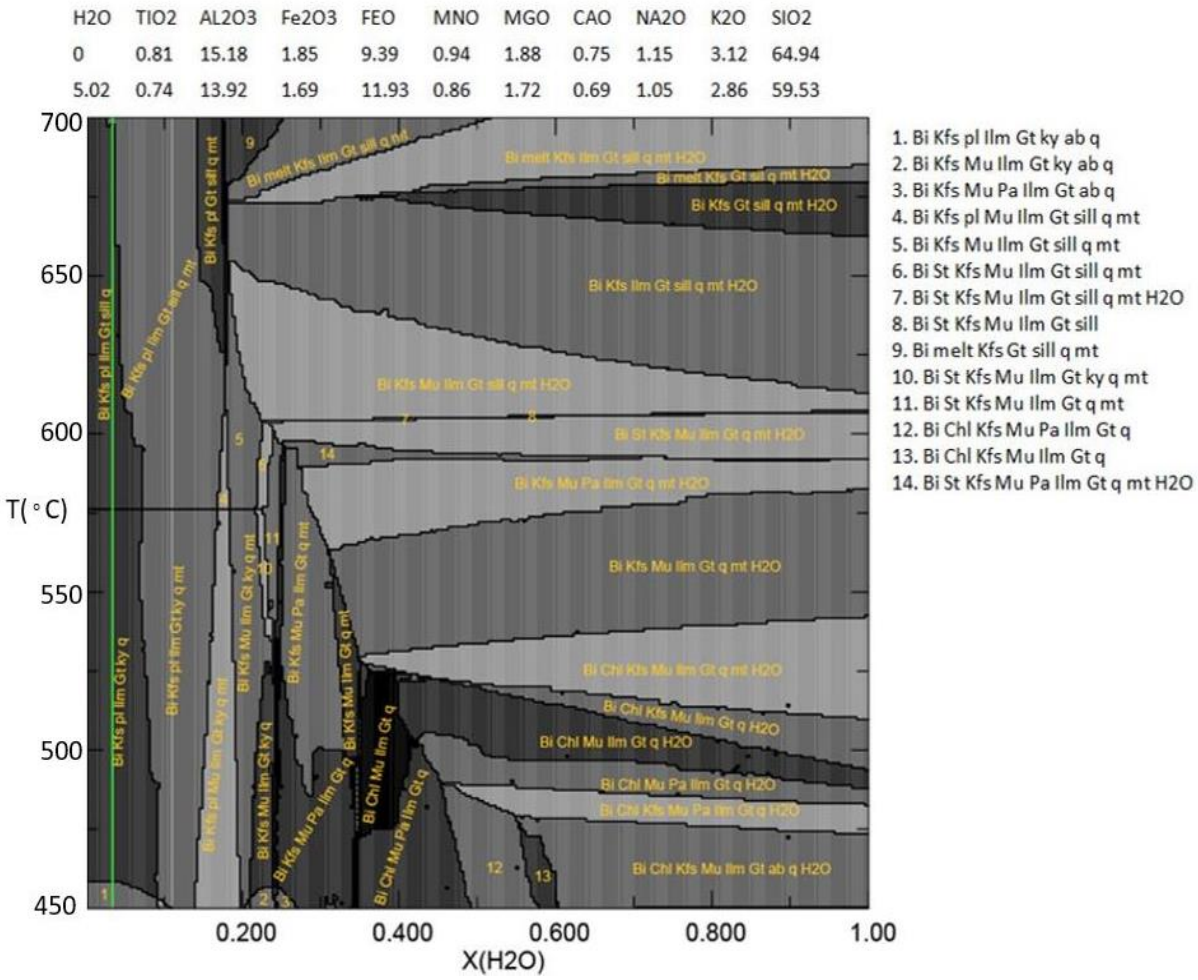

Figure 12. *T*–M_{H2O} pseudosection for sample BAC28 calculated at 5 kbar. Bulk compositions in wt% oxide provided above the diagram are: top row is for M_{H2O} = 0 (left-hand side of diagram) and bottom row is for M_{H2O} = 1.0 (right-hand side of diagram). Vertical green line indicates bulk composition used for the subsequent *P*–*T* pseudosection. Fields that are too small for a legible label are numbered and the corresponding assemblage is listed to the right of the diagram.

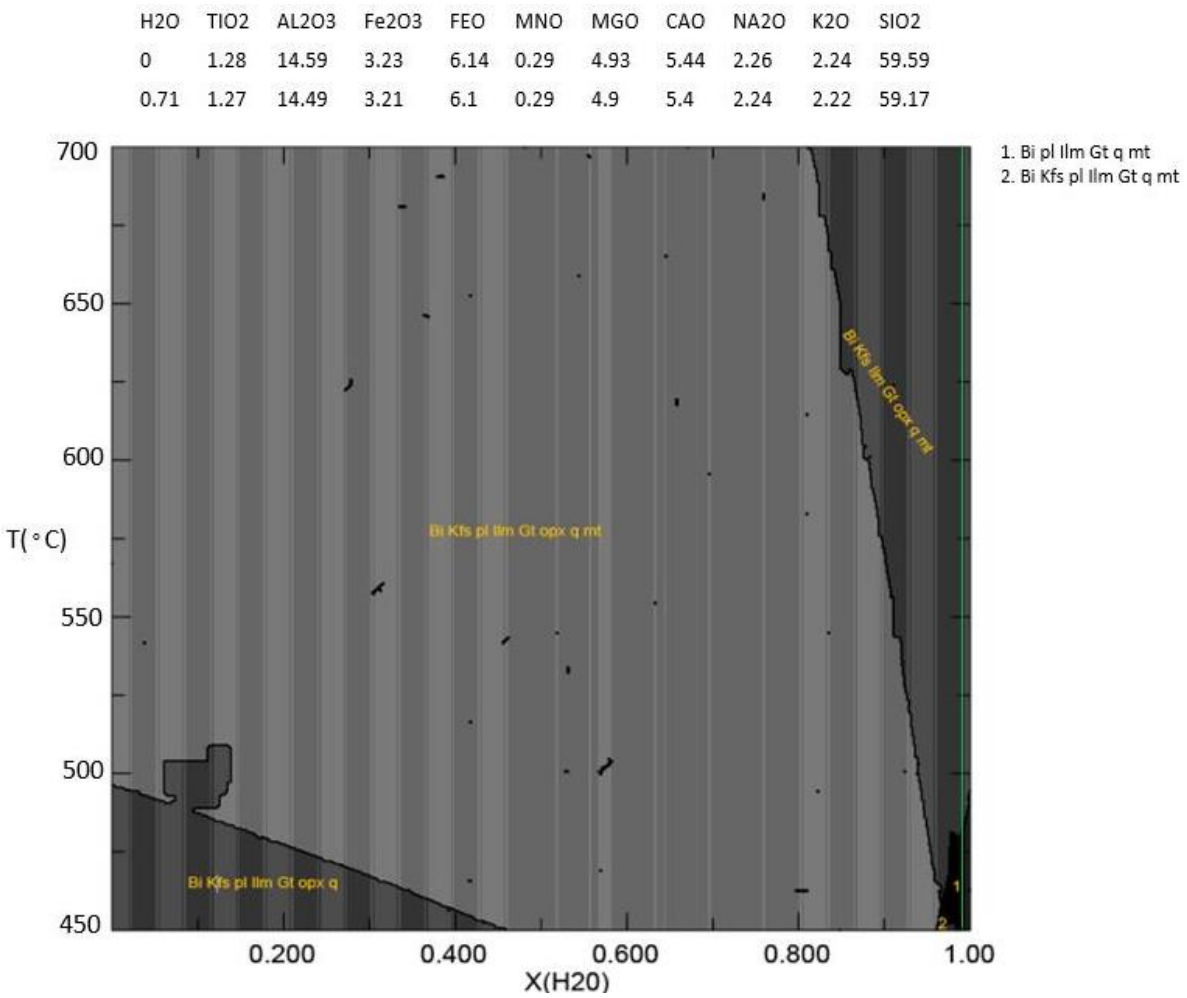

Figure 13. *T*–M_{H2O} pseudosection for sample NDR1 calculated at 5 kbar. Bulk compositions in wt% oxide provided above the diagram are: top row is for M_{H2O} = 0 (left-hand side of diagram) and bottom row is for M_{H2O} = 1.0 (right-hand side of diagram). Vertical green line indicates bulk composition used for the subsequent *P*–*T* pseudosection. Fields that are too small for a legible label are numbered and the corresponding assemblage is listed to the right of the diagram.

4.4.3 Pressure–temperature conditions

Pressure–temperature pseudosections were calculated for three metapelites, BAC23, BAC28 and NDR1 (Figures 14, 15 and 16, respectively). The interpreted peak assemblage fields were contoured for ca (g) (= Ca/(Mg + Fe^{2+} + Mn + Ca) cations = X_{grs}). These calculated compositional values were then compared to measured electron microprobe data for garnet cores, in order to attempt to more tightly constrain peak metamorphic conditions within the peak assemblage field.

Sample BAC23

The peak assemblage garnet + sillimanite + biotite + quartz + plagioclase + ilmenite ± magnetite is stable over the range 2.6 to 7.4 kbar and 550 to 700 °C (Figure 14). The peak assemblage field is bound to higher temperatures by the incoming of silicate melt, and to lower temperatures and higher pressures by the replacement of sillimanite by kyanite or andalusite. The lower-pressure bound on the stability of the peak assemblage is defined by the appearance of cordierite. Garnet is absent at conditions ranging from ~1.0 to 3.9 kbar and 460°C to 700°C and this garnet absent field ('V' shaped) widens up-pressure as temperature increases. Sillimanite stability begins at ~4.2 kbar and 550°C, with its 'V' shaped field widening up-temperature.

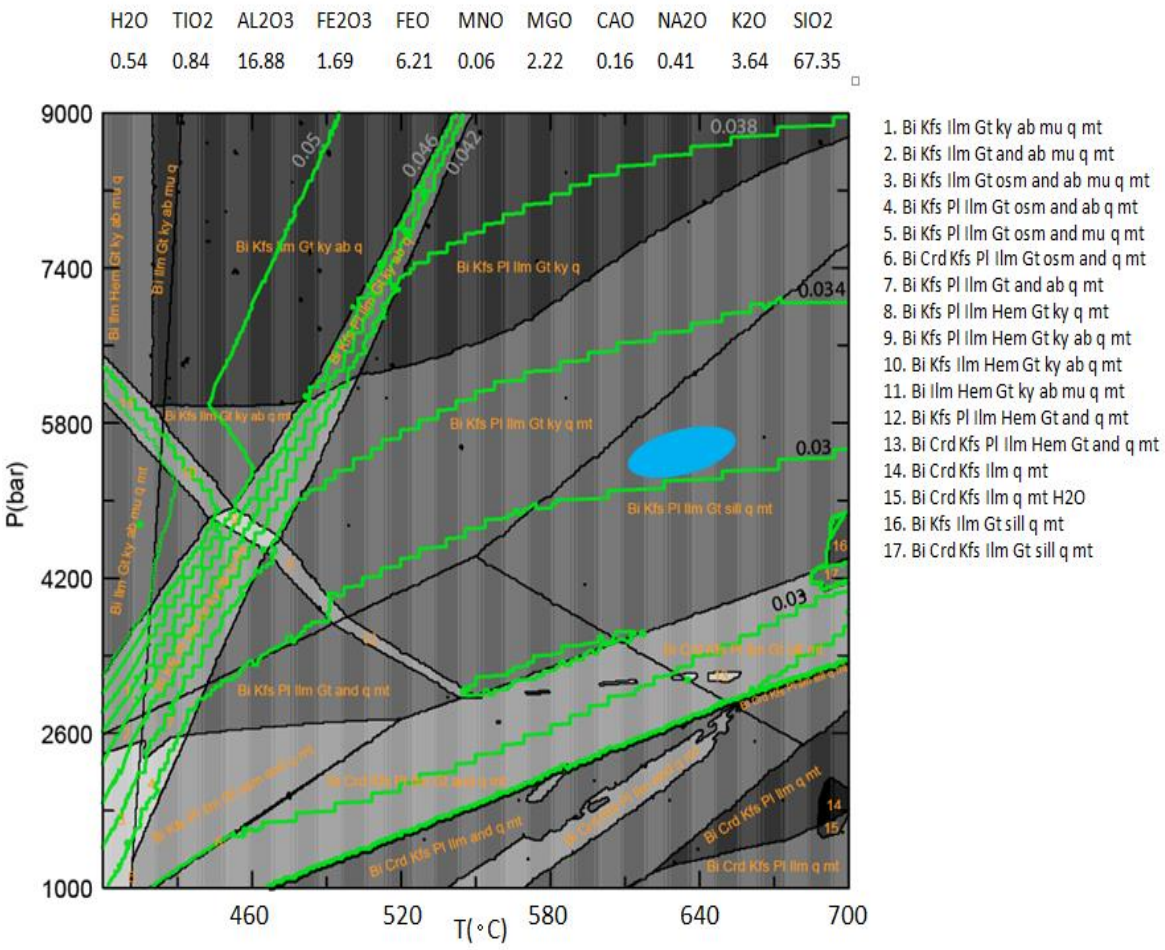

Figure 14. *P–T* pseudosection for sample BAC23. The wt% oxide composition used for calculation of the phase diagram is given above the diagram. Green contours are for the Ca content in garnet, calculated as the ratio of the moles of CaO/(MgO + FeO + CaO + MnO), which is equivalent to the ratio of cations, i.e. Ca/(Ca + Fe^{2+} + Mn + Mg) = X_{grs}. The Ca content of garnet, X_{grs}, is labelled in black and grey numbering next to contours. The blue elipes is located inside the peak assemblage field and is positioned on the basis of matching the calculated chemistry of garnet to the measured (by EPMA) chemistry of garnet.

Sample BAC28

The peak assemblage biotite + garnet + sillimanite + potassium feldspar + plagioclase + ilmenite + magnetite is stable over the range 2.6 to 7.4 kbar and 520 to 700 °C (Figure 15). The peak assemblage field is bound to higher temperatures by the incoming of silicate melt, and to lower temperatures and higher pressures by the replacement of sillimanite by kyanite or andalusite. The

lower-pressure bound on the stability of the peak assemblage is defined by the appearance of cordierite. The *P–T* pseudosection shares numerous similarities with that of BAC23—particularly that of the stability of kyanite, sillimanite and andalusite—owing to the similarity in peak metamorphic assemblages. Garnet is stable across all of modelled *P–T* space in BAC28.

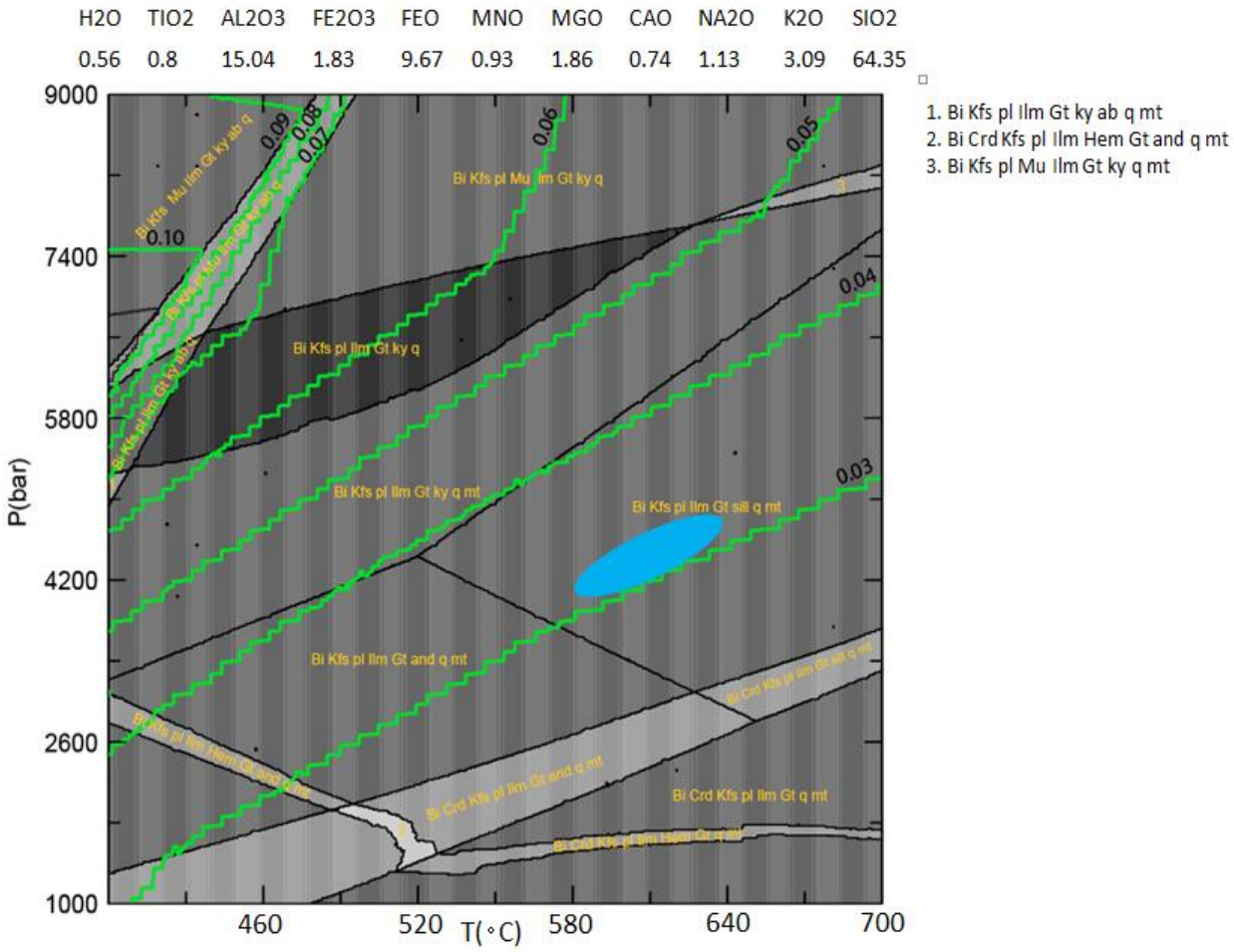

Figure 15. *P–T* pseudosection for sample BAC28. The wt% oxide composition used for calculation of the phase diagram is given above the diagram. Green contours are for the Ca content in garnet, calculated as the ratio of the moles of CaO/(MgO + FeO + CaO + MnO), which is equivalent to the ratio of cations, i.e. Ca/(Ca + Fe^{2+} + Mn + Mg) = X_{grs}. The Ca content of garnet, X_{grs}, is labelled in black numbering next to contours. The blue elipes is located inside the peak assemblage field and is positioned on the basis of matching the calculated chemistry of garnet to the measured (by EPMA) chemistry of garnet.

Sample NDR1

The peak assemblage garnet + biotite + plagioclase + potassium feldspar + ilmenite + quartz is stable over the narrow range 8.2 to 8.7 kbar and 450 to 475 °C (Figure 16). Garnet is stable across all modelled *P–T* space.

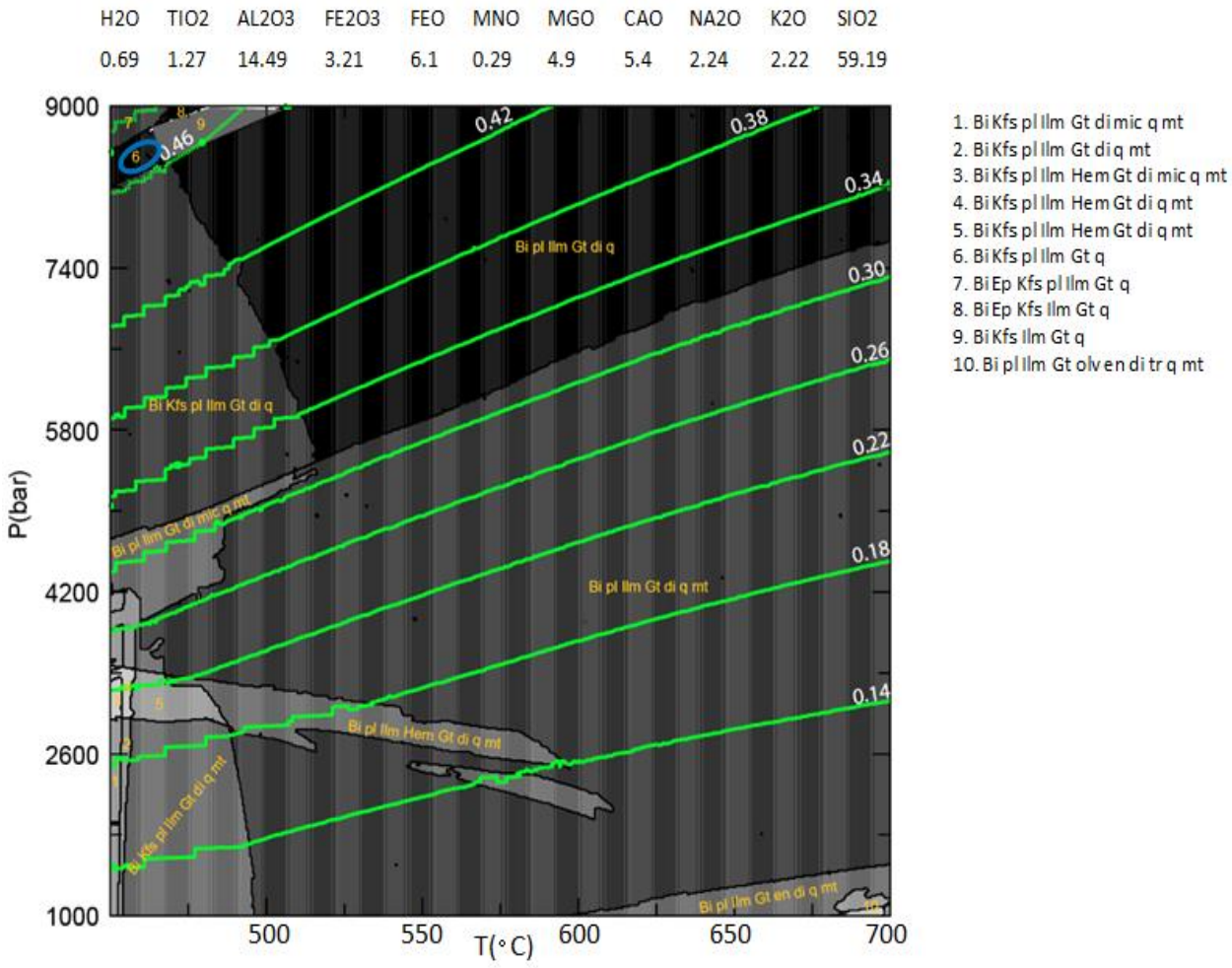

Figure 16. P–T pseudosection for sample NDR1. The wt% oxide composition used for calculation of the phase diagram is given above the diagram. Green contours are for the Ca content in garnet, calculated as the ratio of the moles of CaO/(MgO + FeO + CaO + MnO), which is equivalent to the ratio of cations, i.e. Ca/(Ca + Fe^{2+} + Mn + Mg) = X_{grs}. The Ca content of garnet, X_{grs}, is labelled in white numbering next to contours. The blue elipes is located inside the peak assemblage field and is positioned on the basis of peak mineral assemblage.

5. DISCUSSION

The above results constrain the age and thermal regime (as apparent thermal gradient) of metamorphism in the Fowler Domain, for the purpose of placing possible constraints on the tectonic setting at the time of metamorphism. These results are discussed in the context of existing data and models for the tectonic setting of the Gawler Craton and other parts of Proterozoic Australia. Owing to the different timelines defined by the age data, this discussion will necessarily focus on those two timelines, i.e. the Kimban and Kararan events.

5.1 Monazite U–Pb geochronology

Monazite is a geochronometer that is understood to be reasonably reactive within metamorphic rocks (eg. Williams, 2001; McFarlane *et al.*, 2006; Högdahl *et al.*, 2012; Rubatto *et al.*, 2013) particularly because it rarely survives as a detrital mineral above temperatures of ~350 °C (eg. Janots *et al.*, 2008; Wing *et al.*, 2003). Therefore, in the majority of metamorphic rocks, including rocks in this study, monazite can be interpreted as metamorphic in origin.

The new U–Pb age data collected and presented in here is the first for sample BAC28. This sample contains a metamorphic monazite age population at 1735 ± 19 Ma. The new age data for samples BAC23 (1701 ± 8 Ma) and NDR1 (1599 ± 11 Ma) are significantly older than previous work by Thomas *et al.* (2008) and Howard *et al.* (2011a) whom published monazite U–Pb weighted average ages of 1666 ± 17 Ma (BAC23), and 1505 ± 14 Ma (NDR1) (Table 2). The source of this discrepancy appears to be analytical in nature. Thomas *et al.* (2008) do not appear to have adequately accounted for spectral overlaps between the Th *M*γ peak on U *M*β and U *Mζ*$_2$ on Pb *M*β in their monazite analyses. This conclusion is based upon the spectral analysis of Dutch *et al.* (2010) for monazite U–Th–Pb chemical dating with the same electron microprobe and the same operating conditions. For the analysed monazite compositions, this resulted in ages that were slightly too young (Thomas *et al.*,

2008). Reprocessing of the original data of Thomas *et al.* (2008) using the spectral overlaps determined by Dutch *et al.* (2010) results in more consistency between the existing EMPA data and the LA–ICP–MS monazite U–Pb ages obtained in Howard *et al.* (2011a). Given that the EMPA age data cannot account for isotopic discordance, the LA–ICP–MS monazite ages are more reliable than the EMPA ages (Howard *et al.*, 2011a).

As shown in Figure 4 and Figure 17, the two samples from the Barton block (BAC23 and BAC28) both yielded ages within the Kimban Orogeny time period (Hand *et al.*, 2007). By contrast, the younger monazite age data from NDR1 in the Nundroo Block occurs within the known time period of the Kararan/Hiltaba event (Hand *et al.*, 2007; Thomas *et al.*, 2008). Therefore, for all samples, the new age data correspond to known times of regional deformation and metamorphism in the Gawler Craton.

Attempts to directly constrain the maximum depositional age of sediments were not conducted in this study due to comprehensive detrital zircon studies already having been done by Howard *et al.* (2011a). That U–Pb age data from detrital zircon grains in metasedimentary rocks of the Fowler Domain, Barton and Colona Blocks, suggests that maximum depositional ages are c. 1698±7 Ma (Tallacootra Shear Zone), between c. 1738 Ma and c. 1717 (Barton Block) Ma and 1760±14 Ma Ma (Colona Block) (Howard *et al.*, 2011a). However, monazite ages can be used to constrain the minimum depositional ages for metasedimentary rocks if they record the timing of metamorphism (Howard *et al.*, 2011a). Existing LA–ICP–MS metamorphic monazite U–Pb ages, and hence minimum depositional ages, for metasedimentary rocks from the Fowler Domain are: c. 1696 Ma to c. 1635 Ma (Barton Block), c. 1690 to 1649 Ma (Colona Block) and c. 1593 Ma to 1505 Ma (Nundroo Block) (Table 2; Howard *et al.*, 2011a), and this study c. 1735 Ma to c. 1701 Ma (Barton Block) and c. 1599 Ma (Nundroo Block) in Table 2. Therefore, the data from this study together with the maximum and

minimum depositional ages from Howard *et al.* (2011a) indicate that sedimentation was occurring prior to and synchronous with the onset of the Kimban Orogeny (Figure 17), as well as further sedimentation possibly occurring after the Kimban Orogeny and, although unconstrained, potentially up to the onset of the Kararan/Hiltaba event.

5.2 Peak *P–T* conditions and apparent thermal gradients

Metamorphic rocks record information about their *P–T* evolution in the mineral assemblages, the chemistry and variation in composition of these minerals, and the microstructural relationships among them (Brown, 2014). The *P–T* evolution, based on these variables, can be useful in a general manner be to infer a possible tectonic setting (Brown, 2001, 2006, 2014).

The peak *P–T* conditions of the three samples in this study are further constrained by comparing the calculated composition of garnet with the measured composition. The use of mineral chemistry to further constrain peak *P–T* conditions is best suited to use of cations that diffuse comparatively slowly (e.g. Ca in garnet; Schwandt *et al.*, 1996; Carlson, 2006; Vielzeuf *et al.*, 2007). The green contours on the *P–T* pseudosections (Figures 14, 15, 16) correspond to the ratio X_{grs} = CaO/(CaO + FeO + MnO + MgO) moles = Ca/(Ca + Fe^{2+} + Mn + Mg) cations, calculated directly by Perple_X and calculated manually for measured (by EPMA) mineral compositions. A comparison of calculated vs measured X_{grs} values for samples BAC23 and BAC28 show a mismatch of only 0.01–0.02. Therefore, for these two samples, the measured mineral chemistry can be used to more tightly constrain the peak *P–T* conditions within the respective peak assemblage fields to occur in the region shown by the blue ellipse in Figures 14 and 15.

For sample NDR1 the calculated and measured X_{grs} values have a large (>0.2) mismatch. Therefore the chemistry of garnet is not useful for more tightly constraining the peak *P–T* conditions for this sample. However, the size of the peak assemblage field is already quite small (Figure 16), which

means that the peak *P–T* conditions are reasonably tightly constrained anyhow. A possible reason for the mismatch between measured and calculated garnet chemistry in NDR1 may be due to the sample containing very coarse-grained (2–5mm) garnet. When cutting a sample that contains coarser grained garnet, it can be difficult to slice straight through the centre of a given garnet grain. This issue propagates inaccuracies when measuring chemistry within the garnet grain as, assuming the chemistry corresponding to peak *P–T* conditions occurs in the geometric centre of the grain, the measured compositions will not, and cannot, reflect that attained by the garnet at the peak of metamorphism.

On the basis of peak *P–T* conditions constrained above using garnet chemistry (BAC23, BAC28) or the small size of the peak assemblage field (NDR1), the calculated apparent thermal gradients for the samples are as follows: ~116–122 °C/kbar for BAC23, ~120–135 °C/kbar for BAC28 and ~50–60 °C/kbar for NDR1. These thermal gradients correspond, respectively, to the hotter part of the 'high *T*/*P* or Barrovian' (BAC23 and BAC28) and 'colder than normal' (or eclogite–high-pressure granulite) subdivisions of *P–T* space (Brown, 2006, 2014; Stüwe, 2007; Kelsey and Hand, 2015).

5.3 Possible tectonic settings at time of metamorphism

Different thermal regimes in Earth's crust, as recorded by the metamorphic rock record, can be interpreted in terms of *possible* different tectonic regimes due to the relationship between surface heat flow, crustal heat production and the constraints they place on crustal thickness (eg. Sandiford *et al.*, 2001; Sandiford and McLaren, 2002). High apparent thermal gradients, such as those recorded in the Barton Block, could be interpreted as relatively thin crust (e.g. Spear, 1993; Vernon & Clarke, 2008) at the time of the Kimban Orogeny. Thin crust is more akin to regions of extension rather than compression (eg. Spear, 1993; Vernon and Clarke, 2008). However, high apparent thermal gradients could also potentially reflect crust that is not overly thickened, which could reflect previously

extended crust being thickened to somewhere in the vicinity of near-normal crustal thickness. The third scenario is that the crust does not record an extensional phase and that the crust was thickened a minor amount during the Kimban Event. As sedimentation is constrained to have occurred in the Fowler Domain in the lead up to, and possibly during the early stages of the onset of the Kimban Event (Howard *et al.*, 2011a), it seems probable that the crust records an extensional phase. Therefore, the high thermal gradients obtained from the metamorphic rock record documented in this study would seem to suggest that the Barton Block records an extensional stage that caused metamorphism, regardless of whether or not later thickening occurred.

By contrast, the apparent thermal gradient calculated for the sample NDR1 from the Nundroo Block is significantly lower, at ~50–60 °C/kbar. This range of values is significantly lower than that documented for the Nundroo Block by Teasdale (1997) (Table 2). This discrepancy is probably due to Teasdale (1997) necessarily conducting conventional thermobarometry in smaller chemical systems (e.g. cation exchange reactions) than the full(er) chemistry of the rock, which modern pseudosection analysis allows. Some of the pitfalls of conventional thermobarometry include (possible) re-equilibration of mineral compositions with cooling, issues relating to accounting for Fe^{3+} in minerals (e.g. biotite, ilmenite), only using a small subset of the total mineral assemblage for thermobarometry, not knowing whether the measured mineral compositions combined together to perform conventional thermobarometry are actually in equilibrium, not knowing whether the derived *P*–*T* conditions actually occur inside the stability field of the assemblage, and the circular need to estimate *P* in order to calculate *T* and vice versa (Fitzsimons and Harley, 1994; Kelsey *et al.*, 2003; Powell and Holland, 2008). The presence of garnet in two-pyroxene-bearing mafic granulites from the Nundroo Block adds some circumstantial support to the pressures being comparatively high (eg. Schuhmacher *et al.*, 1990), and thus apparent thermal gradients being comparatively lower, in the Nundroo Block (assuming the mafic granulites have Kararan/Hiltaba metamorphic ages) than

the Barton Block. Apparent thermal gradients of the magnitude calculated in this study are interpreted as the hallmark of Proterozoic convergent orogens (eg. Brown, 2006, 2007, 2014). Therefore, the simplest interpretation is that the metasediments of the Nundroo Block record a convergent tectonic setting at the time of the Kararan/Hiltaba event.

Teasdale (1997) dissected the evolution of the Fowler Domain into three main tectonothermal episodes. Episode 1: between ~1740–1690 Ma, sedimentary sequences were intruded by voluminous sheets, sills and plutons at c. 1740 Ma. This was followed by compressional deformation metamorphism (greenschist–amphibolite facies) at c. 1710 Ma. Later at c. 1690 Ma further voluminous intrusions of granitoid plutons and sheets is documented. Episode 2: between ~1585–1490 Ma, voluminous plutons and sheets intruded parts of the Fowler Domain between ~1585–1560 Ma, which coincide with Kararan/Hiltiba time lines (Creaser, 1996; Peucat *et al.*, 2002; Wade *et al.*, 2006; Betts *et al.*, 2007). Between ~1560–1540 Ma the eastern Fowler Domain experienced compressional deformation and subsequent metamorphism from amphibolite–granulite facies. During the interval ~1540–1490 Ma further deformation occurred followed by felsic magmatism at ~1490 Ma. Episode 3: between ~1200–1100 Ma at least two generations of shear zones developed during transpressional tectonic movements and defines the current architecture of the domain. Teasdale (1997) observations for episode 1 and later part of episode 2 are supported by data collected in this study and is consistent with extension and convergence respectively.

5.4 Tectonic interpretations from elsewhere in Gawler Craton

Having documented Kimban-aged and Kararan-/Hiltaba-aged metamorphism in the Fowler Domain, the following discussion explores how these events have been documented and interpreted elsewhere in the Gawler Craton.

There has been conflicting interpretations surrounding the tectonic regimes of the Gawler Craton during the Kimban Orogeny time line. Past workers have interpreted this period as being compressional and others as extensional. Vassallo and Wilson (2002) suggest that the Kimban Orogeny was undergoing a transpressional tectonic regime by using structural features (folding) as evidence from the Kalinjala Shear Zone (S-SE Gawler Craton). Whereas others have interpreted the west-northwest Gawler Craton (Karari shear zone, western boarder of the Fowler Domain) during this period as a time of extension (Stewart and Betts, 2010; Fraser *et al.*, 2012). This is evident in the sedimentary precursors to the paragneisses of the Nawa Domain which were deposited at c. 1740–1720 Ma (north Gawler Craton) (Payne *et al.*, 2006), then further buried and metamorphosed during the Kimban Orogeny (Fraser *et al.*, 2012), and coincident with high heat flow typical of extended/thinned crust (Stewart and Betts, 2010).

The time line of the Kararan-/Hiltaba orogenic-/magmatic events also possesses conflicting arguments for the Gawler Craton, within the literature. The earlier (c. 1620–1608 Ma) Hiltiba magmatic event has been argued to be plume related (Peucat *et al.*, 2002), and commonly interpreted as an anorogenic event with some tectonic reactivation accompanying this event (McLean and Betts, 2003; Hand *et al.*, 2007). Other workers suggest a series of back-arc intrusions distal to a subduction zone (Creaser, 1996; Wade *et al.*, 2006; Betts *et al.*, 2007). This interpretation is later agued, that subduction related (convergence) Hiltiba aged St Peter Suite overrode an oceanic

hotspot, combined with the overlying lithosphere, and was responsible for the distal deformation by the Isan-Olarian orogenisis and the Hiltiba magmatism (Betts *et al.*, 2009).

Convergence during the Kararan time line (c. 1600–1550 Ma) has also been interpreted for the Gawler Craton. Using structural interpretations Fraser *et al.* (2012) argue that thrusting (crustal thickening) resulting in significant exhumation of marginal domains of the Gawler Craton to the north of the Karari Shear Zone was occurring, and a crustal shortening tectonic regime is also documented in Armit *et al.* (2012) at this time.

Past studies regarding the Fowler Domain (Teasdale, 1997; Daly *et al.*, 1998b; Dawson *et al.*, 2002; Direen *et al.*, 2005; Betts *et al.*, 2008; Thomas *et al.*, 2008) suggest that the deformation and metamorphism during the Paleo-Mesoproterozoic was that of subduction related (convergent) tectonic regime.

5.5 Possible implications for Proterozoic Australia

Since this study has documented Kimban and Kararan/Hiltaba-aged metamorphism from the Fowler Domain, it is instructive to explore thermal gradients and the tectonic interpretations that have been made for these timelines elsewhere in Proterozoic Australia. Both these timelines are recognised as important in the context of debates about the assembly and evolution of the Australian continent (Myers *et al.*, 1996; Betts and Giles, 2006).

There is evidence that suggests the Strangways Metamorphic Complex has undergone at least two cycles of burial and exhumation in a broadly convergent setting at the southern margin of the North Australian Craton (Maidment *et al.*, 2005). Critically however, there is evidence of significant sedimentation in intracontinental basins, in the east–northeast of the South Australian Craton (Curnamona Province), attributed to rifting/extension during the time period corresponding to the

Kimban Orogeny (Barovich and Hand, 2008; Reid and Hand, 2012). Curnamona sedimentation is in the form of Willlyama Supergroup basin associated sediments (Barovich and Hand, 2008; Reid and Hand, 2012). It possesses geochemical characteristics of syn-depositional bimodal magmatism that are indicative of a continental rift environment (Ashley *et al.*, 1996; Rutherford *et al.*, 2006), which support arguments of extension at the time, in Curnamona Province.

Thermal gradients obtained from the Mt Woods inlier (~150–133 °C/kbar) (Boger and White, 2003; Kelsey *et al.*, 2003), are thought to be akin to the Curnamona Province, Coober Pedy Ridge, and Mable Creek Ridge, within the South Australian Craton (Forbes *et al.*, 2012), and are coincident with Kimban aged metamorphism with peak metamorphic ages of 1736 ± 13 Ma (Finlay, 1993; Fanning, 1993). These are interpreted to be high-temperature metamorphism (Finlay, 1993; Fanning, 1993; Daly *et al.*, 1998a) and consistent with an extensional tectonic regime (Brown, 2001, 2006, 2014). The apparent thermal gradients and metamorphic ages from the Barton Block, Fowler Domain from this study support the *idea* of extension during this time line.

During the Kararan/Hiltaba event time lines there are studies which support convergent tectonic settings during a period of orogenisis and hotspot-plume related magmatism (Creaser, 1996; Peucat *et al.*, 2002; McLean and Betts, 2003; Wade *et al.*, 2006; Betts *et al.*, 2007; Hand *et al.*, 2007; Armit *et al.*, 2012; Fraser *et al.*, 2012). Studies focussing on the Kararan event time line based on interpretations from structural observations have argued the event as convergent (Fraser *et al.*, 2012; Armit *et al.*, 2012). This is supported by apparent thermal gradients and metamorphic ages from the Nundroo Block, Fowler Domain in this study.

It is *probable* based on the analyses from this study, that the Gawler Craton and perhaps the entire eastern edge of Proterozoic Australia was undergoing a ‘concertina’ type tectonic regime perhaps similar to that of the later (c. 515–230 Ma) Tasmanides of eastern Australia (Kemp *et al.*, 2009;

Phillips and Offler, 2011) which records transient periods of convergence in an overall extensional setting. The long-lived tectonic regime of the Tasmanides is related to subduction trench retreat with intermittent periods of subduction trench advance, where for example seamounts may 'lock up' subduction for a time producing orogenesis and HPLT rocks (Nundroo Block *P*–*T* conditions). Once this seamount is finally subducted or becomes mechanically separated from the downgoing plate the system will return to back-arc extension via slab/trench roll back producing HTLP rocks (Barton Block *P*–*T* conditions), and accompanying geothermal gradients via back arc extension/basins as recorded in the Willyama Supergroup, Curnamona Province.

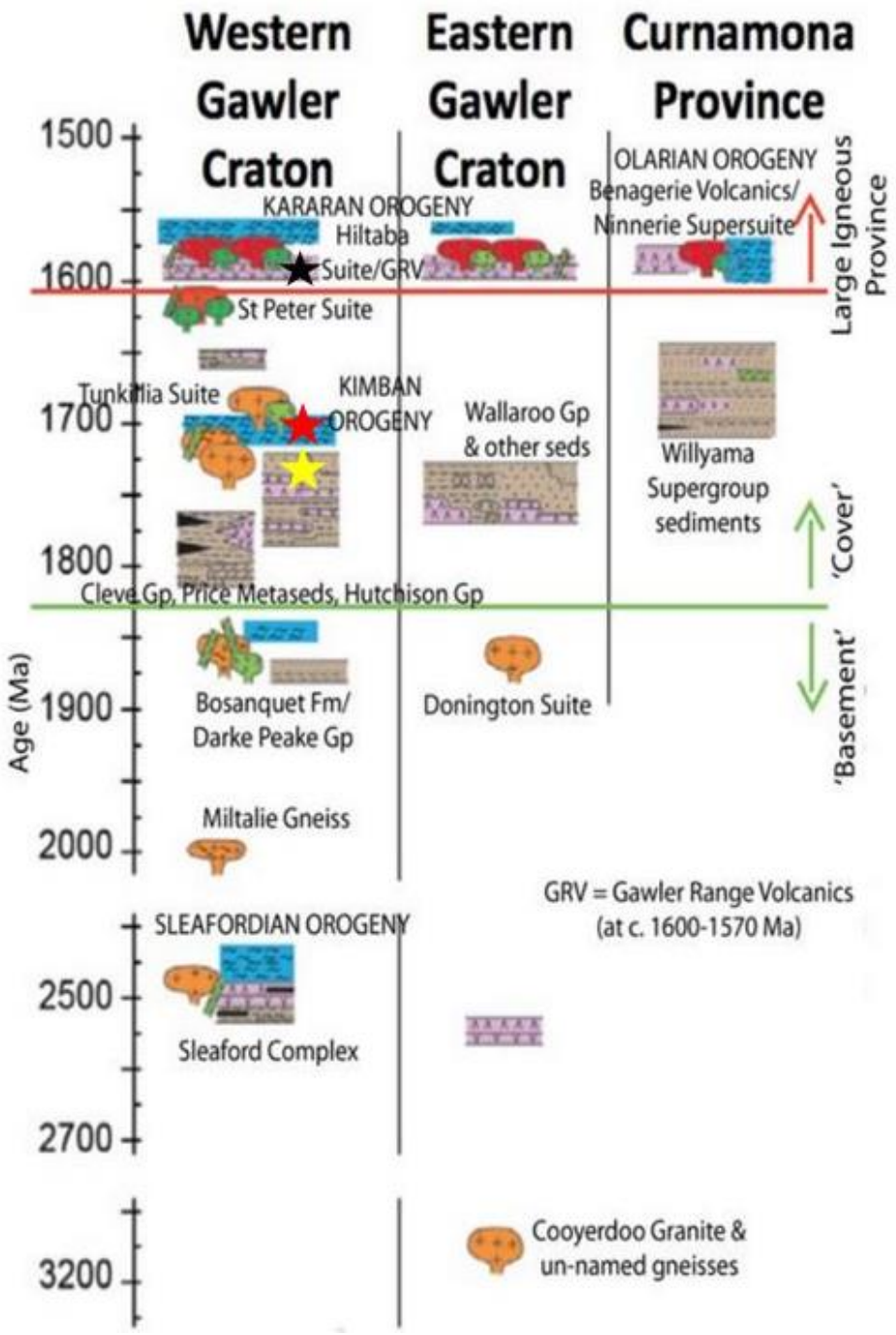

Figure 17. Time–space plot for the southern Gawler Craton. The division into western Gawler Craton vs eastern Gawler Craton (which includes Yorke Peninsula) shows sedimentation of the Willyama Supergroup was partly synchronous with the Kimban Orogeny. Coloured stars are ages from this study, yellow star is sample BAC28 (1735 ± 19 Ma), red star is sample BAC23 (1701 ± 0.8 Ma) and black star is sample NDR1 (1599 ± 11 Ma). Key to data geological history represented in the plot: Brown = sedimentation, orange = felsic–intermediate intrusive rocks, red = Hiltaba suite A-type intrusive rocks, green = mafic intrusive rocks, pink = extrusive magmatism; blue = deformation and metamorphism. Adapted after Reid and Hand (2012).

6. CONCLUSIONS

U-Pb ages are Kimban and Kararan/Hiltaba event aged, recording two metamorphic events within the Fowler Domain. These ages are significant as they are older than recognised in Thomas *et al.* (2008), and extend on work performed by Howard *et al.* (2011a). Apparent thermal gradients in the Fowler Domain produced striking differences, with the Barton Block suggestive of extension whereas the Nundroo Block suggests later convergence. Fowler Domain apparent thermal gradients compared with tectonic interpretations from the Curnamona Province and other areas within the Gawler Craton and Proterozoic Australia during the time periods c.1730-1690 Ma (Kimban), c. 1620–1608 Ma (Hiltiba) and c. 1600–1550 Ma (Kararan) are similar in some cases. This adds to the notion that the Fowler and perhaps the entire Gawler Craton was undergoing overall extension during intermittent times of convergence throughout Proterozoic Australia similar to a Tasmanide type of tectonic evolution. To add further substance to this idea, it is suggested that future work utilise a greater suite of samples from the Fowler Domain and other parts of the Gawler Craton, using methods presented here. This study provides new insight for Proterozoic tectonic regime, by providing a temporal framework using additional monazite geochronology and a thermal framework using phase equilibria forward modelling.

ACKNOWLEDGMENTS

Supervisors David Kelsey and Martin Hand are thanked for their invaluable and ongoing support, guidance and encouragement. Laura Morrissey and Naomi Tucker are thanked for their assistance with Thermocalc phase equilibria modelling. Ben Wade, Aoife McFadden and Angus Netting, Adelaide Microscopy, are thanked for their assistance with SEM imaging, electron probe micro analysis, and LA-ICP-MS analyses.

REFERENCES

ALLEN S. R., MCPHIE J., FERRIS G. & CADD A. G. 2008 Evolution and architecture of a large felsic igneous province in western Laurentia: the 1.6 Ga Gawler Range Volcanics, South Australia., *Volcanology and Geothermal Research,* **172**, 132-147.
ARMIT R. J., BETTS P. G., SCHAEFER B. F. & AILLERES L. 2012 Constraints on long-lived Mesoproterozoic and Palaeozoic deformational events and crustal architecture in the northern Mount Painter Province, Australia, *Gondwana Research,* **22**, 207-226.
ASHLEY P. M., COOK N. D. J. & FANNING C. M. 1996 Geochemistry and age of metamorphosed felsic igneous rocks with A-type affinities in the Willyama Supergroup, Olary Block, South Australia, and implications for mineral exploration, *Lithos,* **38**, 167-184.
BAROVICH K. & HAND M. 2008 Tectonic setting and provenance of the Paleoproterozoic Willyama Supergroup, Curnamona Province, Australia: Geochemical and Nd isotopic constraints on contrasting source terrain components, *Precambrian Research,* **166**, 318-337.
BETTS P. G. & GILES D. 2006 The 1800–1100Ma tectonic evolution of Australia, *Precambrian Research,* **144**, 92-125.
BETTS P. G., GILES D., FODEN J., SCHAEFER B. F., MARK G., PANKHURST M. J., FORBES C. J., WILLIAMS H. A., CHALMERS N. C. & HILLS Q. 2009 Mesoproterzoic plume-modified orogenisis in eastern Precambrian Australia, *Tectonics,* **TC3006**.
BETTS P. G., GILES D. & SCHAEFER B. F. 2008 Comparing 1800-1600 Ma accretionary and basin processes in Australia and Laurentia: possible geographic connections in Columbia, *Precambrian Research,* **166**, 81-82.
BETTS P. G., GILES D., SCHAEFER B. F. & MARK G. 2007 1600-1500 hotspot track in eastern Australia: implications for Mesoproterozoic continental reconstructions, *Terra Nova,* **19**, 496-501.
BOGER S. 2011 Antartica-Before and after Gondwana, *Gondwana Research,* **19**, 335-371.
BOGER S. D. & WHITE R. W. 2003 The metamorphic evolution of metapelitic granulites from Radok Lake, northern Prince Charles Mountains, east Antarctica: evidence for an anticlockwise P–T path. , *Journal of Metamorphic Geology* **21**, 285– 298.
BROWN M. 2001 From microscope to mountain belt: 150 years of petrology and its contribution to understanding geodynamics, particularly the tectonics of orogens, *Journal of Geodynamics,* **32**, 115-164.
BROWN M. 2006 Duality of thermal regimes is the distinctive characteristic of plate tectonics since the Neoarchean, *Geology,* **34**, 961-964.
BROWN M. 2007 Metamorphism, Plate Tectonics, and the Supercontinent Cycle, *Earth Science Frontiers,* **14**, 1-18.
BROWN M. 2014 The contribution of metamorphic petrology to understanding lithosphere evolution and geodynamics, *Geoscience Frontiers,* **5**, 553-569.
CARLSON W. D. 2006 Rates of Fe, Mg, Mn, and Ca diffusion in garnet, *American Mineralogist,* **91**, 1-11.
CONNOLLY J. A. D. 2005 Computation of phase equilibria by linear programming: A tool for geodynamic modeling and its application to subduction zone decarbonation., *Earth and Planetary Science Letters* **236**, 524-541.
CONNOLLY J. A. D. & PETRINI K. 2002 An automated strategy for calculation of phase diagram sections and retrieval of rock properties as a function of physical conditions., *Journal of Metamorphic Geology* **20**, 697-708.
CONOR C. 1995 Moonta-Wallaroo region: An interpretation of the geology of the Maitland and Wallaroo 1:100 000 sheet areas: South Australia Department of Primary Industries and Resources, *Open File Envelope* **8886**, p.537
CREASER R. A. 1996 Petrogenesis of a Mesoproterozoix quartz latite-granitoid suite from the Roxby Downs area, South Australia, *Precambrian Research,* **79**, 371-394.
CUTTS K., HAND M. & KELSEY D. E. 2011 Evidence for early Mesoproterozoic (ca. 1590 Ma) ultrahigh-temperature metamorphism in southern Australia, *Lithos,* **124**, 1–16.
DALY S. J. & FANNING C. M. 1993 Archaean. In: The Geology of South Australia; Volume 1, The Precambrian (eds Drexel, J.F., Preiss, W.V. & Parker, A.J.), *Geological Survey of South Australia Bulletin,* **54**, 32-49.
DALY S. J., FANNING C. M. & FAIRCLOUGH M. C. 1998a Tectonic evolution and exploration potential of the Gawler Craton South Australia, *AGSO Journal of Australian Geology and Geophysics,* **17**, 145-168.
DALY S. J., FANNING C. M. & FAIRCLOUGH M. C. 1998b Tectonic evolution and exploration potential of the Gawler Craton, South Australia, *AGSO Journal of Australian Geology & Geophysics,* **17**, 145-168.

DALY S. J., TONKIN D. G., PURVIS A. & SHI Z. 1994 Colona drilling program, *Mines & Energy South Australia, Open File Envelope,* **8768**.
DAWSON G. C., KRAPEZ B., FLETCHER I. R., MCNAUGHTON N. J. & RASMUSSEN B. 2002 Did late Paleoproterozoic assembly of proto-Australia involve collision between the Pilbara, Yilgarn and Gawler Cratons? Geochronological evidence from the Mount Barren Group in the Albany-Fraser Orogen of Western Australia *Precambrian Research,* **118**, 195-220.
DIREEN N. G., CADD A. G., LYONS P. & TEASDALE J. P. 2005 Architecture of Proterozoic shear zones in the Christie Domain, western Gawler Craton, Australia: geophysical appraisal of poorly exposed orogenic terrane., *Precambrian Research,* **142**, 28-44.
DUCLAUX G., REY P., GUILLOT S. & MENOT R. P. 2007 Orogenparallel flow during continental convergence: numerical experiments and Archean field examples, *Geology,* **35**, 715-718.
DUTCH R. A. 2009 Reworking the Gawler Craton: Metamorphic and geochronologic constraints on Palaeoproterozoic reactivation of the southern Gawler Craton, Australia, *The University of Adelaide, Unpublished PhD thesis*, p.233.
DUTCH R. A., HAND M. & KELSEY D. E. 2010 Unravelling the tectonothermal evolution of reworked Archean granulite facies metapelites using in situ geochronology: an example from the Gawler Craton, Australia, *Journal of Metamorphic Geology,* **28**, 293-316.
FANNING C. M. 1993 Ion-microprobe U–Pb Zircon Dating of the Mount Woods Inlier, Preliminary Results (unpub), *Research School of Earth Sciences, Australian National University,* **8**.
FANNING C. M., FLINT R. B., PARKER A. J., LUDWIG K. R. & BLISSETT A. H. 1988 Refined Proterozoic evolution of the Gawler Craton, South Australia, through U-Pb zircon geochronology, *Precambrian Research,* **40–41**, 363-386.
FANNING C. M., OLIVER R. L. & COOPER J. A. 1981 The Carnot Gneisses, southern Eyre Peninsula, *Quarterly Geological Notes, Geological Survey of South Australia,* **80**, 7-12.
FANNING C. M., REID A. J. & TEALE G. S. 2007 A geochronological framework for the Gawler Craton, South Australia. , *South Australia Geological Survey, Bulletin,* **55**, p.258.
FINLAY J. 1993 Structural interpretation of the Mount Woods Inlier. Unpub, *Honours thesis, Monash University*.
FITZSIMONS I. C. W. & HARLEY S. L. 1994 The influence of retrograde cation-exchange on granulite P–T estimates and a convergence technique for the recovery of peak metamorphic conditions, *Journal of Petrology* **35**, 543-576.
FLINT R. B., BLISSETT A. H., CONOR C. H. H., COWLEY W. M., CROSS K. C., CREASER R. A., DALY S. J., KRIEG G. W., MAJOR R. B., TEALE G. S. & PARKER A. J. 1993 Mesoproterozoic. In: Drexel, J.f., Preiss, W.V., Parker, A. J. (Eds.), The geology of South Australia vol. 1 The Precambrian., *Geological Survey of South Australia Bulletin, Adelaide,* **54** 106-169.
FORBES C. J., GILES D., HAND M., BETTS P. G., SUZUKI K., CHALMERS N. & DUTCH R. 2011 Using P–T paths to interpret the tectonothermal setting of prograde metamorphism: An example from the northeastern Gawler Craton, South Australia, *Precambrian Research,* **185**, 65-85.
FORBES C. J., GILES D., JOURDAN F., SATO K., OMORI S. & BUNCH M. 2012 Cooling and exhumation history of the northeastern Gawler Craton, South Australia, *Precambrian Research,* **200–203**, 209-238.
FRASER G., REID A. & STERN R. 2012 Timing of deformation and exhumation across the Karari Shear Zone, north-western Gawler Craton, South Australia, *Australian Journal of Earth Sciences,* **59**, 547-570.
FRASER G. L. & LYONS P. 2006 Timing of Mesoproterozoic tectonic activity in the northwestern Gawler Craton constrained by 40Ar/39Ar geochronology, *Precambrian Research,* **151**, 160-184.
FRASER G. L. A. N., N.L 2010 New SHRIMP U-Pb zircon ages from the Gawler Craton and Curnamona Province, South Australia, 2008 – 2010. , *Geoscience Australia, Record*.
GILES D., AILLÉRES L., JEFFRIES D., BETTS P. & LISTER G. 2006 Crustal architecture of basin inversion during the Proterozoic Isan Orogeny, Eastern Mount Isa Inlier, Australia, *Precambrian Research,* **148**, 67-84.
GILES D., BETTS P. G. & LISTER G. S. 2004 1.8–1.5-Ga links between the North and South Australian Cratons and the Early–Middle Proterozoic configuration of Australia, *Tectonophysics,* **380**, 27-41.
GRIFfiN W. L., BELOUSOVA E. A., SHEE S. R., PEARSON N. J. & O'REILLY S. Y. 2004 Archean crustal evolution in the northern Yilgarn Craton: U–Pb and Hf-isotope evidence from detrital zircons, *Precambrian Research* **131**, 231-282.
HAND M., REID A. & JAGODZINSKI L. 2007 Tectonic Framework and Evolution of the Gawler Craton, Southern Australia, *Economic Geology,* **102**, 1377-1395.
HÖGDAHL K., MAJKA J., SJÖSTRÖM H., NILSSON K. P., CLAESSON S. & KONEČNÝ P. 2012 Reactive monazite and robust zircon growth in diatexites and leucogranites from a hot, slowly cooled orogen: implications for the

Palaeoproterozoic tectonic evolution of the central Fennoscandian Shield, Sweden, *Contributions to Mineralogy and Petrology,* **163**, 167-188.
HOLLAND T. J. B. & POWELL R. 2011 An improved and extended internally consistent thermodynamic dataset for phases of petrological interest, involving a new equation of state for solids. , *Journal of Metamorphic Geology* **29**, 333-383.
HOWARD H. M., HAND M., BAROVICH K. M., REID A., WADE B. P. & BELOUSOVA E. A. 2009 Detrital zircon ages: improving interpretation via Nd and Hf isotopic data., *Chemical Geology,* **262**, 277-292.
HOWARD K. E., HAND M., BAROVICH K. M., PAYNE J. L. & BELOUSOVA E. A. 2011a U–Pb, Lu–Hf and Sm–Nd isotopic constraints on provenance and depositional timing of metasedimentary rocks in the western Gawler Craton: Implications for Proterozoic reconstruction models, *Precambrian Research,* **184**, 43-62.
HOWARD K. E., HAND M., BAROVICH K. M., PAYNE J. L., CUTTS K. A. & BELOUSOVA E. A. 2011b U-Pb zircon, zircon Hf and whole-rock Sm-Nd isotopic constraints on the evolution of Paleoproterozoic rocks in the northern Gawler Craton, *Australian Journal of Earth Sciences,* **58**, 615-638.
JANOTS E., ENGI M., BERGER J., ALLAZ J., SCHWARZ O. & SPANDLER C. 2008 Prograde metamorphic sequence of REE minerals in pelitic rocks of the Central Alps: implications for allanite–monazite–xenotime phase relations from 250 to 610 °C, *Journal of Metamorphic Geology* **26**, 509-526.
KELSEY D. E. & HAND M. 2015 On ultrahigh temperature crustal metamorphism: Phase equilibria, trace element thermometry, bulk composition, heat sources, timescales and tectonic settings, *Geoscience Frontiers,* **6**, 311-356.
KELSEY D. E., WHITE R. W. & POWELL R. 2003 Orthopyroxene–sillimanite–quartz assemblages: distribution, petrology, quantitative P–T–X constraints and P–T paths, *Journal of Metamorphic Geology* **21**, 439-453.
KEMP A. I. S., HAWKESWORTH C. J., COLLINS W. J., GRAY C. M. & BLEVIN P. L. 2009 Isotopic evidence for rapid continental growth in an extensional accretionary orogen: The Tasmanides, eastern Australia, *Earth and Planetary Science Letters,* **284**, 455-466.
KIRKLAND C. L., SPAGGIARI C. V., PAWLEY M. J., WINGATE M. T. D., SMITHIES R. H., HOWARD H. M., TYLER I. M., BELOUSOVA E. A. & POUJOL M. 2011 On the edge: U–Pb, Lu–Hf, and Sm–Nd data suggests reworking of the Yilgarn craton margin during formation of the Albany-Fraser Orogen, *Precambrian Research* **187**, 223-247.
KORHONEN F. J., POWELL R. & STOUT J. H. 2012 Stability of sapphirine + quartz in the oxidized rocks of the Wilson Lake terrane, Labrador: calculated equilibria in NCKFMASHTO., *Journal of Metamorphic Geology,* **30**, 21-36.
MAIDMENT D. W., HAND M. & WILLIAMS I. S. 2005 Tectonic cycles in the Strangways Metamorphic Complex, Arunta Inlier, central Australia: geochronological evidence for exhumation and basin formation between two high-grade metamorphic events*, *Australian Journal of Earth Sciences,* **52**, 205-215.
MCFARLANE C. R. M., CONNELLY J. N. & CARLSON W. D. 2006 Contrasting response of monazite and zircon to a high-T thermal overprint, *Lithos,* **88**, 135-149.
MCLEAN M. A. & BETTS P. G. 2003 Geophysical constraints of shear zones and geometry of the Hiltiba Suite granites in the western Gawler Craton, Australia, *Australian Journal of Earth Sciences,* **50**, 525-541.
MORRIS B. J., HILL P. W. & FERRIS G. M. 1994 Barton bedrock drilling project, *Mines & Energy South Australia, Report Book,* **163**, p.92.
MORRISSEY L. J., HAND M. & KELSEY D. 2015 Multi-stage metamorphism in the Rayner-Eastern Ghats Terrane: P-T-t constraints from the northern Prince Charles Mountains, east Antartica, *Precambrian Research,* **267**, 137-163.
MORTIMER G. E., COOPER J. A. & OLIVER R. L. 1988 The geochemical evolution of Proterozoic granitoids near Port Lincoln in the Gawler orogenic domain of South Australia, *Precambrian Research,* **40-41**, 387-406.
MYERS J. S., SHAW R. D. & TYLER I. M. 1996 Tectonic evolution of Proterozoic Australia, *Tectonics,* **15**, 1431-1446.
PAYNE J. L., BAROVICH K. M. & HAND M. 2006 Provenance of metasedimentary rocks in the northern Gawler Craton, Australia: Implications for Palaeoproterozoic reconstructions, *Precambrian Research,* **148**, 275-291.
PAYNE J. L., HAND M., BAROVICH K. M., REID A. & EVANS D. A. D. 2009 Correlations and reconstruction models for the 2500–1500 Ma evolution of the Mawson Continent, *Geological Society, London, Special Publications,* **323**, 319-355.
PAYNE J. L., HAND M., BAROVICH K. M. & WADE B. P. 2008 Temporal constraints on the timing of high-grade metamorphism in the northern Gawler Craton: implications for assembly of the Australian Proterozoic, *Australian Journal of Earth Sciences,* **55**, 623-640.

PEUCAT J. J., CAPDEVILA R., FANNING C. M., MENOT R. P., PECORA L. & TESTUT L. 2002 1.6 Ga felsic volcanic blocks in the moraines of the Terre Adelie Craton, Antartica: comparisons with the Gawler Range Volcanics, Aouth Australia., *Australian Journal of Earth Sciences,* **49**, 831-845.
PEUCAT J. J., MÉNOT R. P., MONNIER O. & FANNING C. M. 1999 The Terre Adélie basement in the East-Antarctica Shield: geological and isotopic evidence for a major 1.7 Ga thermal event; comparison with the Gawler Craton in South Australia, *Precambrian Research,* **94**, 205-224.
PHILLIPS G. & OFFLER R. 2011 Contrasting modes of eclogite and blueschist exhumation in a retreating subduction system: The Tasmanides, Australia, *Gondwana Research,* **19**, 800-811.
PISAREVSKY S. A., ELMING S.-Å., PESONEN L. J. & LI Z.-X. 2014 Mesoproterozoic paleogeography: Supercontinent and beyond, *Precambrian Research,* **244**, 207-225.
POWELL R. & HOLLAND T. J. B. 1998 An internally consistent dataset with uncertainties and correlations: 3. Applications to geobarometry, worked examples and a computer program. , *Journal of Metamorphic Geology* **6**, 173-204.
POWELL R. & HOLLAND T. J. B. 2008 On thermobarometry, *Journal of Metamorphic Geology* **29**, 155-179.
POWELL R., WHITE R. W., GREEN E. C. R., HOLLAND T. J. B. & DIENER J. F. A. 2014 On parameterising thermodynamic descriptions of minerals for petrological calculations., *Journal of Metamorphic Geology* **32**, 245-260.
REID A. & HAND M. 2012 Mesoarchean to Mesoproterozoic evolution of the southern Gawler Craton, South Australia, *Episodes,* **35**.
REID A., HAND M., JAGODZINSKI E., KELSEY D. & PEARSON N. 2008 Paleoproterozoic orogenesis in the southeastern Gawler Craton, South Australia, *Australian Journal of Earth Sciences,* **55**, 449-471.
REID A. J., JAGODZINSKI E. A., ARMIT R. J., DUTCH R. A., KIRKLAND C. L., BETTS P. G. & SCHAEFER B. F. 2014a U-Pb and Hf isotopic evidence for Neoarchean and Paleoproterozoic basement in the buried northern Gawler Craton, South Australia, *Precambrian Research,* **250**, 127-142.
REID A. J., JAGODZINSKI E. A., FRASER G. L. & PAWLEY M. J. 2014b SHRIMP U–Pb zircon age constraints on the tectonics of the Neoarchean to early Paleoproterozoic transition within the Mulgathing Complex, Gawler Craton, South Australia, *Precambrian Research,* **250**, 27-49.
RUBATTO D., CHAKRABORTY S. & DASGUPTA S. 2013 Timescales of crustal melting in the Higher Himalayan Crystallines (Sikkim, Eastern Himalaya) inferred from trace element-constrained monazite and zircon chronology, *Contributions to Mineralogy and Petrology,* **165**, 349-372.
RUTHERFORD L., BAROVICH K. & CLARK C. 2006 Continental ca 1.7-1.69 Ga Fe-rich metaholeiitses in the Curnamona Province, Australia: a record of melting of a heterogeneous, subduction-modified lithospheric mantle', *Australian Journal of Earth Sciences,* **53**, 501-519.
SANDIFORD M., HAND M. & MCLAREN S. 2001 Tectonic feedback, intraplate orogeny and the geochemical structure of the crust; a central Australian perspective. In: Miller, J.A., Holdsworth, R.E., Buick, I.S., Hand, M. (Eds), Continental reactivation and reworking., *Geological Society, London, Special Publications,* **184**, 195-218.
SANDIFORD M. & MCLAREN S. 2002 Tectonic feedback and the ordering of heat producing elements within the continental lithosphere, *Earth and Planetary Science Letters,* **204**, 133-150.
SAYERS J., SYMONDS P. A., DIREEN N. G. & BERNARDEL G. 2001 Nature of the continent-ocean transition on the non-volcanic rifted margin of the central Great Australian Bight, *Geological Society, London, Special Publications,* **187**, 51-76.
SCHUHMACHER R., SCHENK W., RAASE P. & VITANAGE P. W. 1990 Granulite facies metamorphism of metabasic and intermediate rocks in the Highland Series of Sri Lanka. In: Brown, M. and Ashworth, J. (ed.): High-grade metamorphism and crustal anatexis, *Allen and Unwin, London,* , 235 -271.
SCHWANDT C. S., CYGAN R. T. & WESTRICH H. R. 1996 Ca self-diffusion in grossular garnet *American Mineralogist,* **81**, 448-451.
SMITHIES R. H., HOWARD H. M., EVINS P. M., KIRKLAND C. L., KELSEY D. E., HAND M., WINGATE M. T. D., COLLINS A. S. & BELOUSOVA E. 2011 High-temperature granite magmatism, crust–mantle interaction and the Mesoproterozoic intracontinental evolution of the Musgrave Province, central Australia, *Journal of Petrology* **52**, 931-958.
SPEAR F. S. 1993 Metamorphic phase equilibria and pressure–temperature–time paths, *Monograph, Mineralogical Society of America, Washington, D.C.*
STEWART J. R. & BETTS P. G. 2010 Implications for Proterozoic plate margin evolution from geophysical analysis and crustal-scale modeling within the western Gawler Craton, Australia, *Tectonophysics,* **483**, 151-177.
STÜWE K. 2007 Geodynamics of the lithosphere: quantitative description of geological problems, 2nd edition, *Springer-Verlag, Berlin, Heidelberg, Dordrecht*.

SWAIN G. M., HAND M., TEASDALE J., RUTHERFORD L. & CLARK C. 2005 Age constraints on terrane-scale shear zones in the Gawler Craton, southern Australia, *Precambrian Research*, **139**, 164-180.
SZPUNAR M., HAND M., BAROVICH K., JAGODZINSKI E. & BELOUSOVA E. 2011 Isotopic and geochemical constraints on the Paleoproterozoic Hutchison Group, southern Australia: Implications for Paleoproterozoic continental reconstructions, *Precambrian Research*, **187**, 99-126.
TEASDALE J. 1997 Methods for understanding poorly exposed terranes: The interpretive geology and tectonothermal evolution of western Gawler Craton. Ph.D. Thesis. University of Adelaide.
THOMAS J. L., DIREEN N. G. & HAND M. 2008 Blind orogen: Integrated appraisal of multiple episodes of Mesoproterozoic deformation and reworking in the Fowler Domain, western Gawler Craton, Australia, *Precambrian Research*, **166**, 263-282.
VASSALLO J. J. & WILSON C. J. L. 2002 Palaeoproterozoic regional-scale non-coaxial deformation: an example from eastern Eyre Peninsula, South Australia, *Journal of Structural Geology*, **24**, 1-24.
VERNON R. H. & CLARKE G. 2008 Principles of metamorphic petrology, *Cambridge University Press*, p.446.
VIELZEUF D., BARONNET A., PERCHUK A. L., LAPORTE D. & BAKER M. B. 2007 Calcium diffusivity in alumino-silicate garnets: an experimental and ATEM study, *Contributions to Mineralogy and Petrology*, **154**, 153-170.
WADE B. P., BAROVICH K. M., HAND M., SCRIMGEOUR I. R. & CLOSE D. F. 2006 Evidence for early Mesoproterozoic arc magmatism in the Musgrave Block, central Australia: Implications for Proterozoic crustal growth and tectonic reconstructions of Australia *Journal of Geology* **114**, 43-63.
WHITE R. W., POWELL R., HOLLAND T. J. B., JOHNSON T. E. & GREEN E. C. R. 2014a New mineral activity–composition relations for thermodynamic calculations in metapelitic systems, *Journal of Metamorphic Geology*, **31**, 261-286.
WHITE R. W., POWELL R. & JOHNSON T. E. 2014b The effect of Mn on mineral stability in metapelites revisited: new a–x relations for manganese-bearing minerals., *Journal of Metamorphic Geology* **32**, 809-828.
WILLIAMS I. S. 2001 Response of detrital zircon and monazite, and their U–Pb isotopic systems, to regional metamorphism and host-rock partial melting, Cooma Complex, southeastern Australia, *Australian Journal of Earth Sciences*, 557-580.
WING B. A., FERRY J. M. & HARRISON T. M. 2003 Prograde destruction and formation of monazite and allanite during contact and regional metamorphism of pelites; petrology and geochronology, *Contributions to Mineralogy and Petrology*, **145**, 228-250.

APPENDIX A: GEOCHEMISTRY/ MINERAL CHEMISTRY

(a)

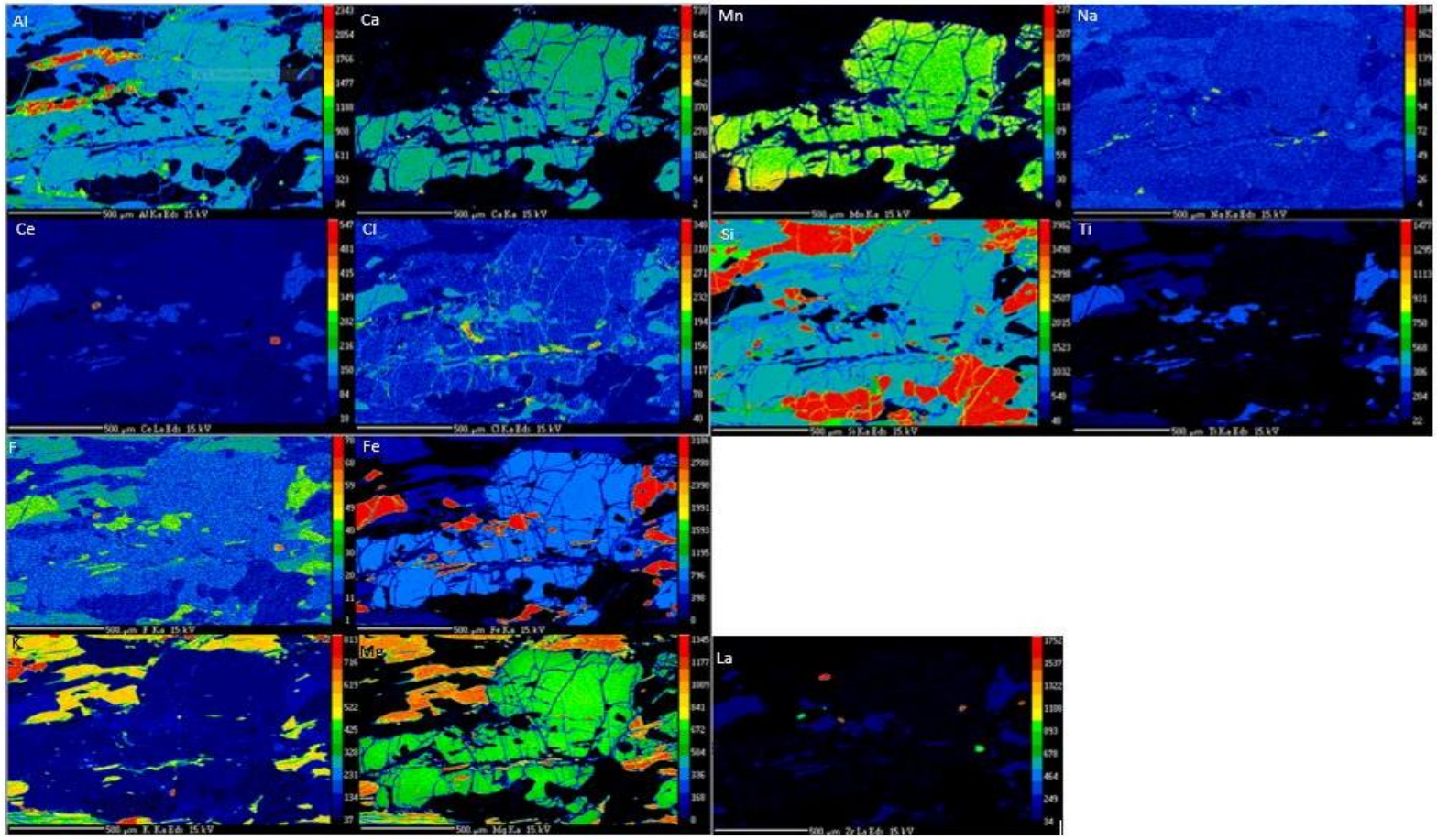

(b)

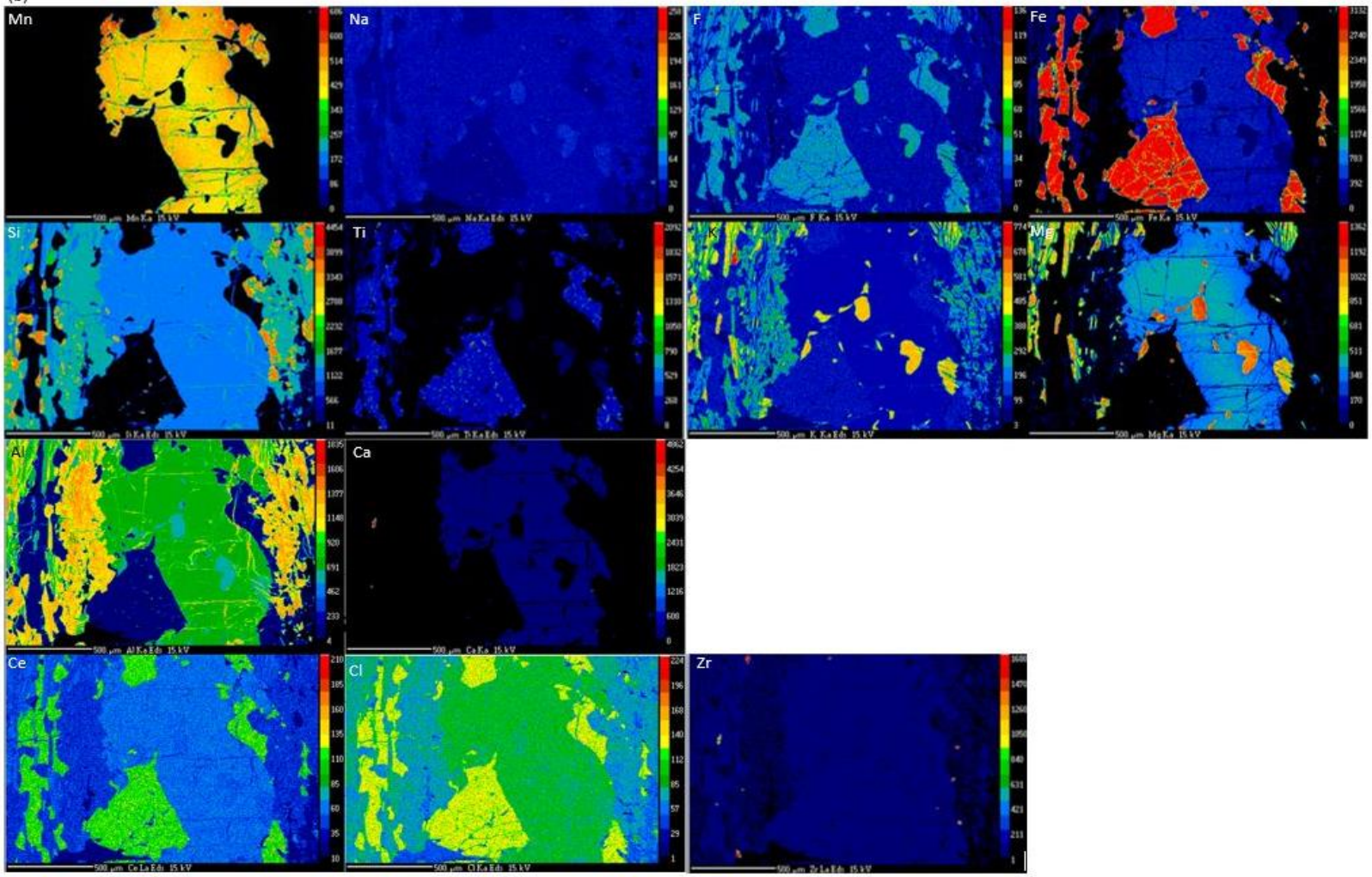

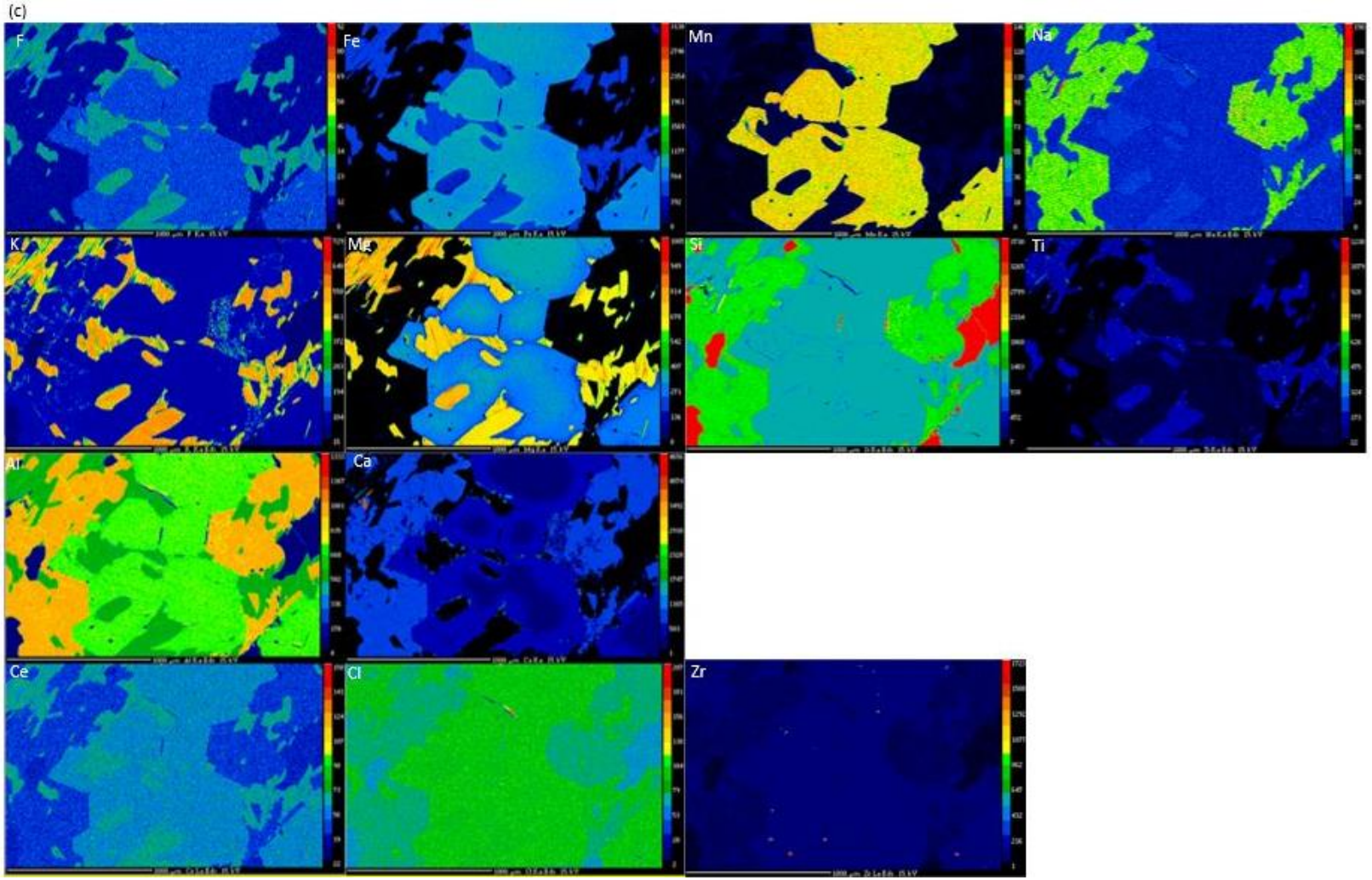

Figure 18. EPMA maps of samples (a) BAC23, (b) BAC28, (c) NDR1. Each map is for concentrations of different elements, labelled on top left corner of each map.

Table 4. EPMA representative analysis for sample BAC23

	BAC23 Area 1					BAC23 Area 2					
Mineral	gt rim	gt core	bi	ilm	sil	gt rim	gt core	bi	ilm	sil	qtz
SiO2	40.038	39.642	37.724	0.000	36.000	39.401	39.699	37.812	0.000	36.764	99.930
TiO2	0.048	0.000	1.757	11.452	0.000	0.000	0.000	1.992	7.693	0.009	0.004
Al2O3	23.408	22.413	17.444	0.224	61.039	22.186	22.196	17.379	0.259	62.262	0.039
Cr2O3	0.006	0.008	0.000	0.093	0.038	0.000	0.043	0.000	0.137	0.008	0.007
FeO	19.223	18.901	7.725	75.724	1.203	20.199	19.584	8.336	79.378	1.165	0.447
MnO	3.529	3.626	0.026	0.008	0.000	4.728	3.979	0.018	0.000	0.000	0.072
MgO	12.817	13.330	20.014	0.065	0.008	11.636	12.566	19.765	0.090	0.015	0.013
ZnO	0.000	0.000	0.000	0.000	0.013	0.000	0.029	0.078	0.000	0.000	0.000
CaO	1.875	1.935	0.033	0.010	0.000	2.015	2.008	0.044	0.009	0.009	0.019
Na2O	0.044	0.029	0.235	0.035	0.018	0.020	0.027	0.225	0.000	0.014	0.000
K2O	0.008	0.001	9.271	0.000	0.004	0.006	0.012	9.586	0.000	0.010	0.001
Cl	0.070	0.000	0.012	0.000	0.000	0.000	0.007	0.026	0.000	0.009	0.000
F	0.036	0.000	0.187	0.216	0.000	0.001	0.000	0.324	0.208	0.000	0.000
Total	101.07	99.89	94.35	87.74	98.32	100.19	100.15	95.44	87.69	100.26	100.53
No. Oxygens	12	12	11	3	5	12	12	11	4	5	2
Si	2.968	2.978	2.735	0.000	0.995	2.984	2.989	2.723	0.000	0.996	0.997
Ti	0.003	0.000	0.096	0.317	0.000	0.000	0.000	0.108	0.293	0.000	0.000
Al	2.045	1.984	1.490	0.010	1.987	1.980	1.970	1.475	0.015	1.987	0.000
Cr	0.000	0.000	0.000	0.003	0.001	0.000	0.003	0.000	0.005	0.000	0.000
Fe2+	1.192	1.187	0.468	2.330	0.028	1.279	1.233	0.502	3.359	0.026	0.004
Mn2+	0.222	0.231	0.002	0.000	0.000	0.303	0.254	0.001	0.000	0.000	0.001
Mg	1.416	1.493	2.163	0.004	0.000	1.314	1.411	2.122	0.007	0.001	0.000
Zn	0.000	0.000	0.000	0.000	0.000	0.000	0.002	0.004	0.000	0.000	0.000
Ca	0.149	0.156	0.003	0.000	0.000	0.164	0.162	0.003	0.001	0.000	0.000
Na	0.006	0.004	0.033	0.003	0.001	0.003	0.004	0.031	0.000	0.001	0.000
K	0.001	0.000	0.857	0.000	0.000	0.001	0.001	0.880	0.000	0.000	0.000
Cl	0.009	0.000	0.001	0.000	0.000	0.000	0.001	0.003	0.000	0.000	0.000
F	0.008	0.000	0.043	0.025	0.000	0.000	0.000	0.074	0.033	0.000	0.000
Total Cations (S)	8.002	8.032	7.847	2.666	3.012	8.027	8.027	7.850	3.680	3.011	1.003

Table 5. EPMA representative analysis for sample BAC28

	BAC28 area 1						BAC28 area 2						
Mineral	gt rim	gt core	bi	ilm	ksp	sil	gt rim	gt core	bi	ilm	sil	qtz	ksp
SiO2	38.443	39.005	38.492	0.000	64.648	51.817	38.760	38.379	38.519	0.105	45.159	100.515	59.303
TiO2	0.000	0.000	1.610	6.679	0.001	0.000	0.009	0.000	2.120	36.675	0.036	0.006	0.002
Al2O3	21.565	21.824	18.445	0.378	19.143	37.449	21.583	21.402	18.752	0.206	37.582	0.056	18.368
Cr2O3	0.000	0.020	0.018	0.074	0.000	0.023	0.000	0.006	0.028	0.092	0.000	0.000	0.005
FeO	12.163	12.450	4.866	81.738	0.028	1.333	11.992	11.841	7.369	50.349	0.609	0.121	0.258
MnO	17.761	16.574	0.152	0.134	0.000	0.028	16.536	18.261	0.325	0.074	0.038	0.000	0.003
MgO	8.434	9.416	21.870	0.103	0.000	0.892	8.512	7.432	19.693	0.045	1.019	0.005	0.235
ZnO	0.006	0.039	0.080	0.000	0.000	0.000	0.000	0.000	0.100	0.025	0.000	0.011	0.000
CaO	2.247	1.856	0.000	0.000	0.122	0.361	2.252	2.225	0.027	0.004	0.028	0.000	0.048
Na2O	0.000	0.010	0.358	0.000	1.761	0.202	0.016	0.023	0.140	0.037	0.050	0.011	0.808
K2O	0.000	0.000	9.582	0.001	14.457	3.074	0.001	0.000	9.727	0.000	0.074	0.007	14.184
Cl	0.001	0.000	0.003	0.000	0.001	0.067	0.001	0.000	0.000	0.000	0.007	0.004	0.000
F	0.015	0.002	0.669	0.195	0.014	0.000	0.000	0.000	0.639	0.121	0.000	0.000	0.000
Total	100.63	101.19	95.86	89.22	100.17	95.23	99.66	99.57	97.17	87.68	84.60	100.74	93.22
No. Oxygens	12	12	11	3	8	5	12	12	11	3	5	2	8
Si	2.972	2.979	2.707	0.000	2.968	1.481	3.004	3.001	2.705	0.003	1.420	0.999	2.937
Ti	0.000	0.000	0.085	0.189	0.000	0.000	0.001	0.000	0.112	0.842	0.001	0.000	0.000
Al	1.965	1.964	1.529	0.017	1.036	1.261	1.971	1.972	1.552	0.007	1.393	0.001	1.072
Cr	0.000	0.001	0.001	0.002	0.000	0.001	0.000	0.000	0.002	0.002	0.000	0.000	0.000
Fe2+	0.786	0.795	0.286	2.572	0.001	0.032	0.777	0.774	0.433	1.284	0.016	0.001	0.011
Mn2+	1.163	1.072	0.009	0.004	0.000	0.001	1.085	1.209	0.019	0.002	0.001	0.000	0.000
Mg	0.972	1.072	2.293	0.006	0.000	0.038	0.984	0.866	2.061	0.002	0.048	0.000	0.017
Zn	0.000	0.002	0.004	0.000	0.000	0.000	0.000	0.000	0.005	0.001	0.000	0.000	0.000
Ca	0.186	0.152	0.000	0.000	0.006	0.011	0.187	0.186	0.002	0.000	0.001	0.000	0.003
Na	0.000	0.001	0.049	0.000	0.157	0.011	0.002	0.003	0.019	0.002	0.003	0.000	0.078
K	0.000	0.000	0.860	0.000	0.847	0.112	0.000	0.000	0.871	0.000	0.003	0.000	0.896
Cl	0.000	0.000	0.000	0.000	0.000	0.003	0.000	0.000	0.000	0.000	0.000	0.000	0.000
F	0.004	0.000	0.149	0.023	0.002	0.000	0.000	0.000	0.142	0.012	0.000	0.000	0.000
Total Cations (S)	8.044	8.039	7.823	2.790	5.015	2.948	8.011	8.014	7.781	2.146	2.885	1.001	5.014

Table 6. EPMA representative analysis for sample NDR1

	NDR1 area 1				NDR1 area 2		
Mineral	gt rim	gt core	bi	pl	gt rim	gt core	mt
SiO2	56.014	38.133	36.354	56.792	37.032	39.176	0.009
TiO2	0.000	0.013	4.476	0.000	5.127	0.007	0.693
Al2O3	27.116	21.375	15.257	27.022	17.896	21.734	0.544
Cr2O3	0.024	0.026	0.019	0.018	0.320	0.040	0.953
FeO	0.040	25.773	14.716	0.056	17.478	24.175	86.977
MnO	0.000	3.289	0.058	0.000	0.361	2.818	0.153
MgO	0.000	7.594	14.590	0.016	12.271	7.707	0.075
ZnO	0.000	0.014	0.022	0.000	0.000	0.004	0.000
CaO	9.316	3.488	0.019	9.012	0.567	5.287	0.055
Na2O	6.490	0.000	0.071	6.479	0.247	0.001	0.020
K2O	0.263	0.000	9.736	0.283	8.455	0.008	0.001
Cl	0.005	0.000	0.000	0.000	0.027	0.000	0.000
F	0.003	0.000	0.343	0.000	0.266	0.000	0.223
Total	99.27	99.70	95.52	99.68	99.93	100.96	89.61
No. Oxygens	12	12	12	8	12	12	4
Si	3.809	2.981	2.960	2.559	2.891	3.002	0.000
Ti	0.000	0.001	0.274	0.000	0.301	0.000	0.027
Al	2.173	1.969	1.464	1.435	1.647	1.963	0.034
Cr	0.001	0.002	0.001	0.001	0.020	0.002	0.039
Fe2+	0.002	1.685	1.002	0.002	1.141	1.549	3.800
Mn2+	0.000	0.218	0.004	0.000	0.024	0.183	0.007
Mg	0.000	0.885	1.771	0.001	1.428	0.880	0.006
Zn	0.000	0.001	0.001	0.000	0.000	0.000	0.000
Ca	0.679	0.292	0.002	0.435	0.047	0.434	0.003
Na	0.856	0.000	0.011	0.566	0.037	0.000	0.002
K	0.023	0.000	1.011	0.016	0.842	0.001	0.000
Cl	0.001	0.000	0.000	0.000	0.004	0.000	0.000
F	0.001	0.000	0.088	0.000	0.066	0.000	0.037
Total Cations (S)	7.543	8.033	8.501	5.015	8.379	8.015	3.918

APENDIX B: LA-ICP-MS GEOCHRONOLOGY

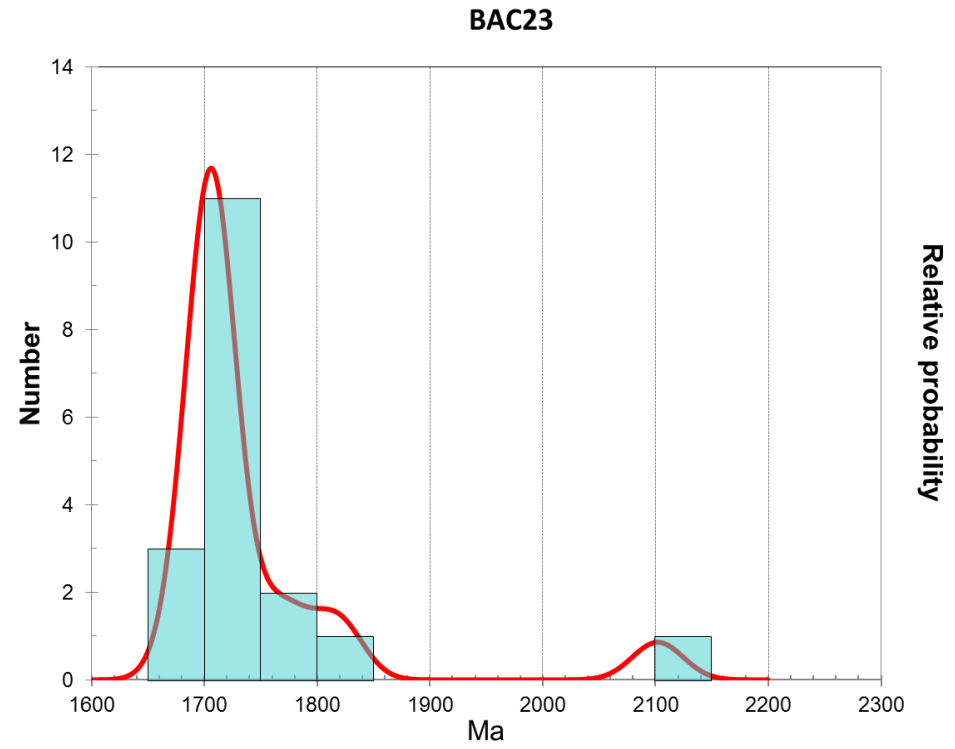

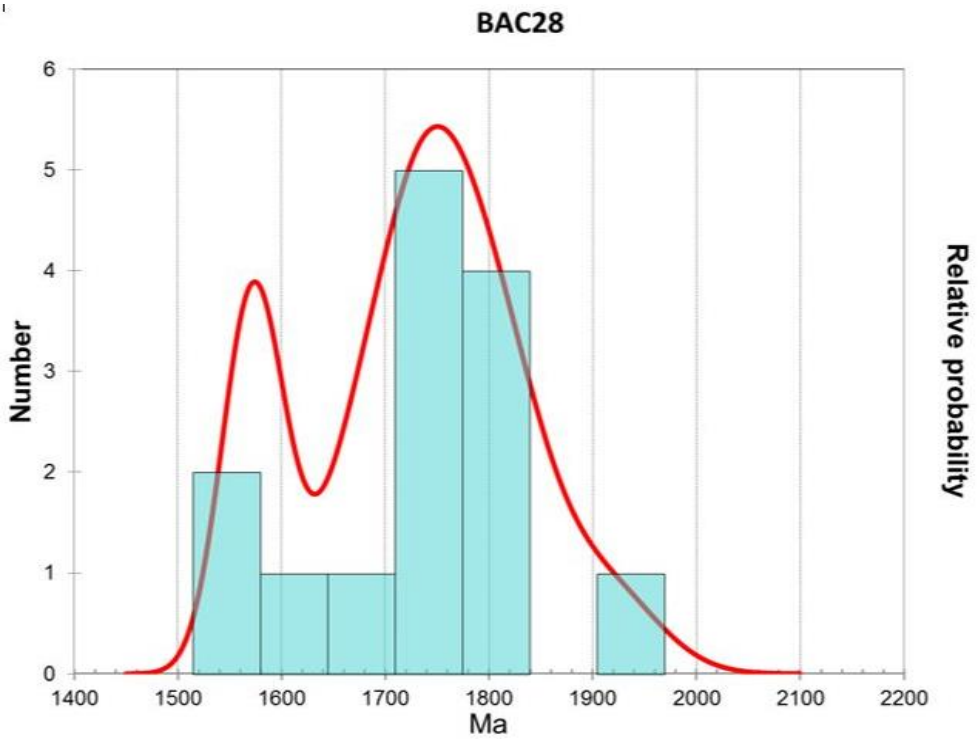

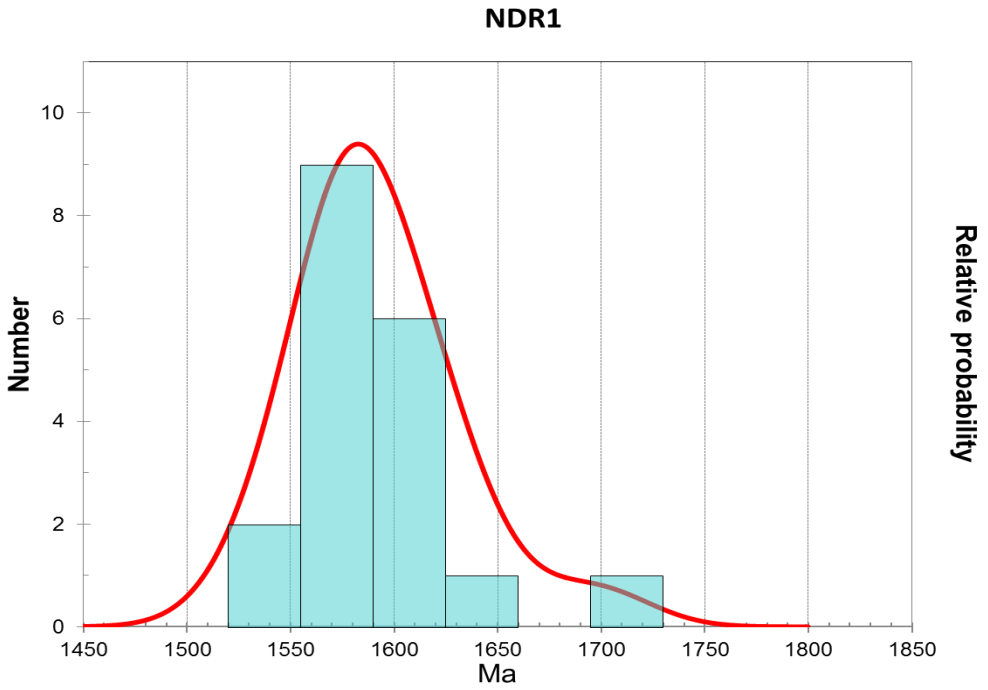

Figure 19. Probability density plots from LA-ICP-MS geochronology.

Table 7. Analysis of unknowns for samples in this study.

Analysis no.	Pb207/U235	1σ	Pb206/U238	1σ	Pb207/Pb206	1σ	Conc.	Pb207/Pb206 age	Pb206/U238 age	Pb207/U235 age
Sample BAC23 (Barton block metapelites)										
BAC23MNZ3	4.38669	0.06969	0.30348	0.00477	0.10489	0.00112	100	1712.5	1712.5	1709.8
BAC23MNZ4	4.43787	0.07082	0.30975	0.00488	0.10397	0.00113	99	1696.1	1696.1	1719.4
BAC23MNZ2	4.52812	0.07176	0.31273	0.00493	0.10508	0.00111	99	1715.6	1715.6	1736.2
BAC23MNZ2A	4.56401	0.07232	0.31686	0.005	0.10452	0.0011	98	1705.9	1705.9	1742.7
BAC23MNZ5	4.43714	0.07086	0.30716	0.00486	0.10483	0.00112	100	1711.4	1711.4	1719.3
BAC23MNZ6	4.29375	0.07094	0.29882	0.00474	0.10428	0.00123	100	1701.6	1701.6	1692.2
BAC23MNZ7	4.53761	0.07922	0.30889	0.00498	0.10662	0.0014	100	1742.3	1742.3	1737.9
BAC23MNZ8	4.21781	0.07044	0.29626	0.0047	0.10332	0.00125	100	1684.5	1684.5	1677.5
BAC23MNZ9	4.37582	0.07065	0.30385	0.00485	0.1045	0.00113	100	1705.6	1705.6	1707.8
BAC23MNZ10	4.45906	0.07282	0.299	0.00478	0.10822	0.00121	102	1769.6	1769.6	1723.4
BAC23MNZ11	4.30051	0.07025	0.2988	0.00479	0.10444	0.00116	100	1704.6	1704.6	1693.5
BAC23MNZ12	4.26523	0.07019	0.29874	0.00479	0.10361	0.00117	100	1689.8	1689.8	1686.7
BAC23MNZ13	4.6718	0.08738	0.30811	0.00509	0.11003	0.00165	102	1799.9	1799.9	1762.2
BAC23MNZ14	5.64399	0.09799	0.31435	0.0051	0.13029	0.00169	109	2101.9	2101.9	1922.8
BAC23MNZ15	4.29329	0.07131	0.29774	0.00482	0.10464	0.00118	101	1707.9	1707.9	1692.1
BAC23MNZ16	4.58423	0.0762	0.29888	0.00478	0.11131	0.00132	104	1820.9	1820.9	1746.4
BAC23MNZ18	4.23877	0.071	0.29472	0.0048	0.10437	0.00119	99	1703.2	1703.2	1681.6
BAC23MNZ19	4.34375	0.0735	0.30032	0.00491	0.10496	0.00122	101	1713.6	1713.6	1701.7
BAC23MNZ20	953.55408	165.0818	7.18803	1.10224	0.96114	0.1253	101	5181.6	5181.6	6966.8

Table 7. continued

Analysis no.	Pb207/U235	1σ	Pb206/U238	1σ	Pb207/Pb206	1σ	Conc.	Pb207/Pb206 age	Pb206/U238 age	Pb207/U235 age
Sample BAC28 (Barton block metapelites)										
MNZ1	4.06933	0.06661	0.30603	0.00441	0.09655	0.00139	116	1558.4	1648.2	1721.1
MNZ2	4.01664	0.06845	0.29872	0.00434	0.09763	0.00149	104	1579.2	1637.6	1684.9
MNZ3	4.13731	0.07117	0.30727	0.00446	0.09776	0.0015	105	1581.8	1661.7	1727.2
MNZ4	4.15187	0.08691	0.29542	0.0046	0.10203	0.00205	103	1661.4	1664.6	1668.6
MNZ5	4.08422	0.07388	0.30052	0.0044	0.09866	0.00162		1599	1651.2	1693.9
MNZ6	5.78093	0.10837	0.32777	0.00484	0.12803	0.0022	101	2071.1	1943.6	1827.6
MNZ7	7.02639	0.13883	0.33016	0.00499	0.15448	0.00286	98	2396.1	2114.8	1839.2
MNZ8	6.33253	0.14959	0.32655	0.0054	0.14076	0.00329	100	2236.6	2023	1821.6
MNZ9	4.39893	0.12862	0.30321	0.00527	0.1053	0.0031	61	1719.6	1712.1	1707.2
MNZ10	4.43766	0.12764	0.30372	0.00524	0.10605	0.00306		1732.6	1719.4	1709.7
MNZ11	4.48583	0.13332	0.30488	0.00526	0.10678	0.00319	98	1745.2	1728.4	1715.5
MNZ12	4.62339	0.10992	0.31806	0.00487	0.10549	0.00241	101	1722.9	1753.5	1780.2
MNZ13	15.73013	0.39943	0.3836	0.00645	0.29759	0.00751	102	3457.7	2860.5	2093.1
MNZ14	4.40053	0.11179	0.30217	0.00469	0.10568	0.0026	100	1726.2	1712.4	1702.1
MNZ15	4.47302	0.11635	0.30338	0.00473	0.10699	0.00271	104	1748.8	1726	1708
MNZ16	4.6968	0.12954	0.30776	0.00486	0.11074	0.00299	103	1811.6	1766.7	1729.7
MNZ17	5.15471	0.14745	0.31886	0.0051	0.1173	0.00331	102	1915.5	1845.2	1784.1
MNZ18	4.60353	0.1358	0.30396	0.00489	0.10989	0.0032	102	1797.6	1749.9	1710.9
MNZ19	4.62201	0.14013	0.30584	0.00494	0.10965	0.00329	102	1793.6	1753.3	1720.2
MNZ20	4.55445	0.14184	0.29919	0.00486	0.11045	0.00342	102	1806.8	1741	1687.3

Table 7. continued

Analysis no.	Pb207/U235	1σ	Pb206/U238	1σ	Pb207/Pb206	1σ	Conc.	Pb207/Pb206 age	Pb206/U238 age	Pb207/U235 age
Sample NDR1 (Nundroo Block metapelites)										
MNZ3	3.95011	0.0671	0.28742	0.00418	0.0997	0.00146	101	1624	1618.6	1628.6
MNZ4	3.82876	0.06358	0.27915	0.00404	0.0995	0.0014	98	1598.8	1614.8	1587.1
MNZ5	3.7475	0.05843	0.2786	0.00397	0.09758	0.00123	100	1581.6	1578.4	1584.3
MNZ6	8.97242	0.33254	0.31371	0.00833	0.20747	0.00852	61	2335.2	2885.9	1758.9
MNZ9	3.76047	0.06695	0.27914	0.00415	0.09772	0.00151	100	1584.3	1581.1	1587
MNZ10	3.70331	0.06689	0.27217	0.00407	0.0987	0.00156	97	1572.1	1599.6	1551.8
MNZ11	3.71453	0.06783	0.27333	0.00411	0.09857	0.00158	98	1574.5	1597.3	1557.7
MNZ12	3.83766	0.06887	0.28379	0.00426	0.09808	0.00152	101	1600.7	1588	1610.4
MNZ13	3.69649	0.06797	0.2791	0.00422	0.09606	0.00154	102	1570.6	1549	1586.8
MNZ14	3.78268	0.09066	0.2794	0.00467	0.09819	0.00227	100	1589.1	1590.1	1588.3
MNZ15	3.89767	0.06225	0.29028	0.00423	0.09738	0.00122	104	1613.2	1574.6	1642.9
MNZ16	3.81523	0.06165	0.28395	0.00416	0.09745	0.00124	102	1596	1575.8	1611.2
MNZ17	4.19202	0.07362	0.30243	0.00455	0.10053	0.00147	104	1672.5	1633.8	1703.3
MNZ18	4.13415	0.07199	0.2882	0.00433	0.10403	0.00149	96	1661.1	1697.2	1632.5
MNZ19	3.81225	0.07138	0.28635	0.0044	0.09655	0.00155	104	1595.3	1558.5	1623.3
MNZ20	4.85635	0.09864	0.26365	0.00426	0.13358	0.00246	70	1794.7	2145.5	1508.5
MNZ21	3.67243	0.06257	0.27833	0.00417	0.09568	0.0013	103	1565.4	1541.6	1583
MNZ22	4.00515	0.07971	0.29223	0.0046	0.09939	0.00173	102	1635.2	1612.6	1652.6
MNZ23	3.80935	0.06974	0.28325	0.00435	0.09752	0.00148	102	1594.7	1577.3	1607.7
MNZ24	3.83075	0.07149	0.28436	0.00439	0.09769	0.00152	102	1599.2	1580.4	1613.3
MNZ25	3.81556	0.07395	0.28368	0.00444	0.09753	0.00161	102	1596	1577.4	1609.9
MNZ26	3.86311	0.07198	0.28528	0.00442	0.09819	0.00151	102	1606	1590	1617.9

APPENDIX C: SCANNING ELECTRON MICROSCOPE (SEM XL-30)

Imaged using: Beam voltage: 20Kv, Spot size 4, imaged in backscatter.

Samples TAL4, BAC 23, NDR1-41m and BAC23 were imaged at Adelaide Microscopy. All 4 samples were imaged on the Philips XL30 Scanning Electron microscope. Imaging was performed in back scatter electron mode (BSE), EDAX software was used to confirm the composition of grains during imaging. The mineral of interest, and close up images of these taken. Also size of monazite grains was noted to discriminate grains that were <40µm (too small for laser ablation). Images were systematically saved so that these photos can be made into a montage at a later date. Sample BAC 23 and 28 was mounted in the SEM using carbon coated tape, and placed perpendicular to the door. The slide was imaged at 69X magnification length ways starting in the bottom right hand corner to produce a total of 45 images. NDR1 was mounted in the same way as BAC samples but placed horizontal to the door so that the slide can be imaged width ways (9 rows and 5 columns). Starting in the top left corner and working right, a total of 99 images were taken at 69X magnification.